Politecnico di Torino

Politecnico di Torino

Corso di Laurea Magistrale in Ingegneria Energetica e Nucleare
A.a. 2020/2021
Sessione di Laurea Luglio 2021

Study of a heat exchanger for heat removal in the ARC fusion reactor

Concept of a sodium heat pipes heat exchanger

Supervisors:

Prof. Massimo Zucchetti
Dr. Raffaella Testoni

Co-supervisors:

Samuele Meschini
Stefano Segantin

Candidate:

Ettore Gastaldi

Content

List of figures

List of tables

Abstract

Il progetto ARC ("Affordable, Robust and Compact reactor") è un design concettuale di un reattore a fusione nucleare sviluppato dal "Massachusetts Institute of Technology (MIT) Plasma Science and Fusion Center". ARC è un tokamak con una potenza pari 200-250 MWe, che utilizza come fluido refrigerante dei sali fusi di fluoro, litio e berillio (FLiBe). Una volta costruito avrà l'obiettivo di diminuire i costi, la complessità e le dimensioni degli impianti a fusione nucleare. Nel presente studio viene proposto un possibile design di uno scambiatore di calore da implementare all'interno di ARC per il trasferimento di calore dal FLiBe ad un fluido secondario, utilizzato all'interno di un ciclo Brayton per la produzione di elettricità. La tecnologia scelta per la costruzione di tale scambiatore sono molteplici heat pipes che usano sodio come fluido termovettore. Dalle analisi numeriche, effettuate con il software Comsol Multiphysics, è risultato che un singolo heat pipe è in grado di scambiare una potenza pari a circa 4.2 kW con aria come fluido secondario. Tale valore può essere incrementato a 8.7 kW usando elio a 25 bar al posto dell'aria, ed applicando delle alette radiali per migliorarne lo scambio termico.

Abstract

ARC ("Affordable, Robust and Compact reactor") is a conceptual design of a nuclear fusion reactor developed by the "Massachusetts Institute of Technology (MIT) Plasma Science and Fusion Center". ARC is a tokamak with a power of 200-250 MWe, which uses molten fluorine salts lithium and beryllium (FLiBe) as coolant. Once built, it will aim to reduce the costs, the complexity and the size of nuclear fusion plants. In the present study will be proposed a possible design of a heat exchanger to be implemented in the ARC design for the heat transfer from the FLiBe to a secondary fluid used within a Brayton cycle for electricity generation. The technology chosen are multiple heat pipes which use sodium as fluid. From the numerical analyzes, carried out with the Comsol Multiphysics software, it was found that a single heat pipe is able to exchange a thermal power of approximately 4.2 kW with air as a secondary fluid. This value can be increased to 8.7 kW by using helium at 25 bar instead of air, and by applying radial fins to improve the heat exchange.

1. Introduction

Compared to today's main projects for the construction of tokamaks, for instance ITER, the ARC reactor [1], under development at Massachusetts Institute of Technology (MIT), is more compact and therefore less expensive, thanks to the use of many innovative technologies and materials [2][3]. The ARC reactor in fact has a major radius of 3.3 m, about half of that of ITER, and a minor radius of 1.1 m which is expected to produce about 200-250 MWe, with a design plasma fusion gain $Q_p \approx 13.6$. Among the different technologies that would make these goals possible, there are certainly the innovations regarding superconducting toroidal field coils: they are made by rare earth barium copper oxide (REBCO), which allows higher operating temperatures with a design point of 20 K, with respect to the superconducting materials used for ITER, allowing the use of other coolants (e.g. liquid hydrogen, liquid neon) compared to the more complicated liquid helium refrigerant system used for ITER. In addition, the toroidal field coils are designed with joints to enable disassembly, allowing to remove the vacuum vessel in order to test different designs and materials, as well as mitigating the damage on the first wall. Another design innovation of the ARC, compared to its predecessors, is the use of a liquid blanket instead of a solid one. The use of fluoride lithium beryllium molten salts (FLiBe) inside the blanket allows to obtain at the same time excellent moderation and neutron shielding, excellent heat removal and a tritium breeding ratio ≥ 1.

Once built, the ARC reactor will have the function of demonstrating that the production of electricity is possible and convenient, using reactors with the characteristics listed above.

For several years nuclear fusion has been described as the sacred grail of energy production, holding the promise to produce abundant and clean energy by using widely available materials. In the case of ARC, as for many other fusion reactors, the materials used to make the fusion reactions take place are deuterium (D) - a heavy form of hydrogen present in nature, for instance in the oceans- and tritium (T), another hydrogen isotope, produced from lithium. The D-T fusion reactions occur at very high temperatures and pressures inside the plasma, a state of matter which can be described as highly ionized gas. These reactions produce particles with a considerable amount of kinetic energy (mainly neutrons) which produce heat

by impacting the wall surrounding the plasma, called blanket. Heat is then extracted by a coolant (FLiBe), which passes inside a heat exchanger in order to heat a secondary fluid (e.g. steam, air or helium), which in turn is used to move the blades of a turbine within a power cycle (e.g. Rankine, Brayton), producing electricity.
The purpose of this study is therefore to design such a heat exchanger, identifying the most suitable technology and simulating its operation and performance under the expected heat loads.
In chapter 2 the operating conditions of the heat exchanger and the possible technologies to be adopted in the application of interest will be described. In the third chapter the heat pipe technology will therefore be introduced, explaining its operating principles and identifying the materials to be used to fulfill different requirements, such as chemical compatibility between the different materials involved and resistance to high temperatures and corrosion. In the following chapter, the operation of the entire heat exchanger composed of multiple heat pipes will first be analyzed, identifying the secondary fluid to be used in the power cycle for the electricity production. Finally, a stationary numerical analysis of a single heat pipe will be conducted, commenting the pressure, speed and temperature profiles obtained as well as the power exchanged, from which the number of heat pipes necessary within the exchanger will be found. In chapter 5 an analysis for the design improvement of the heat pipe will be performed, finding the optimal profile of the fins to improve the heat exchange with the secondary fluid.

2. Heat removal in the ARC fusion reactor

Before going into the details of the design of the heat exchanger, it is necessary to briefly introduce the boundary conditions in which it would work, as well as the tasks it must be able to perform if implemented.

2.1. Operating conditions of the heat exchanger

The ARC reactor is expected to be able to generate around 630 MW of thermal power under nominal conditions, despite its modest size, since the largest radius of the toroid is equal to 3.3 m. To remove this power, a cooling system which uses the eutectic mixture F_4Li_2Be as the heat transfer fluid has been studied. The F_4Li_2Be salts, called FLiBe, are composed by lithium and beryllium fluorides, and in recent years has taken more and more interest since they can be used for a wide range of high temperatures. Other properties that make the FLiBe an excellent compromise for the ARC design are: good thermal conductivity, low chemical reactivity, low electrical conductivity (therefore fewer interactions with the high magnetic fields involved) and finally the moderating and neutron multiplication capacity obtained thanks to the addition of beryllium to the mixture [3][17]. In fact, thanks to the reaction $^{9}Be(n,2n)^{4}He$, beryllium is able to act as a neutron multiplier by increasing the neutron flux and therefore the production of tritium through the reactions $^{6}Li(n,t)^{4}He$ and $^{7}Li(n,t+n)^{4}He$. Figure 1 shows a diagram of the path that the coolant follows inside the reactor [4]. As can be seen in the figure, the FLiBe coming from the heat exchanger enters from the top of the reactor at 800 K [5]. It first cools the first wall through multiple channels, then it passes inside the main FLiBe tank that surrounds the plasma and finally it returns to the heat exchanger.

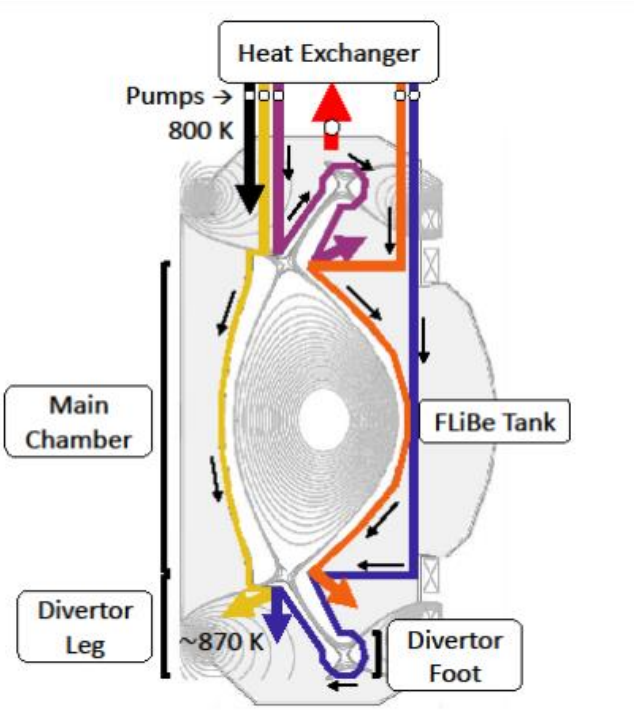

Figure 1. Path of the coolant inside the reactor [4].

The inlet and outlet conditions of the coolant are summarized in Table 1 [5]. The inlet temperature of the salts into the reactor is set at 800 K under nominal conditions to ensure a certain margin over the melting temperature of the FLiBe, equal to 732 K. Regarding the expected exit temperature of the FLiBe from the reactor there is still a high degree of uncertainty, as it depends on the thermal power that the reactor will be able to supply.

Different temperatures can be hypothesized, but recent studies on the integrity of the reactor vacuum vessel suggest not to exceed 880 K to have a long life of the plant. Regarding the speed of the salts, a limit value of 2 m/s has been identified to limit corrosion problems related to salts, although the Nickel alloys used for the blanket walls are quite resistant to corrosion.

Table 1. Inlet and outlet conditions of the FLiBe in the heat exchanger [5].

Properties	Value
Inlet temperature	800 K
Outlet temperature	880 K
Pressure	2 bar
Speed	2.5 m/s

To summarize, the heat exchanger should be able to remove an enormous amount of heat to bring the salts back to a temperature of 800 K, comparable with the amount of thermal power transferred inside the reactor (i.e. 630 MW). In the ARC design there is also a storage system that would allow to solve the problem of intermittency of energy production, as the reactor will produce large quantities of thermal energy in small time intervals, that somehow has to be stored. The implementation of a storage system also allows to reduce the instant power to exchange inside the heat exchanger, and therefore also the number of heat pipes required.

2.2. Possible technologies for heat removal

There are different technologies for heat removal using molten salts as a heat exchange fluid. Some of these technologies have already been used in the past for passive heat removal in some molten salts fission reactors. Three possible technologies to be used within the heat exchanger in question are shown below.

2.2.1. No intermediate loop

No intermediate loop is a concept still under development, proposed for some fission reactors such as LMFBR ("Liquid Metal Fast Breeder Reactors") and FHRs ("Fluoride High Temperature Reactors") [6][7]. The key concept of these exchangers is to eliminate the intermediate loop from the design. Eliminating the intermediate loop, which transfers the heat from the coolant to an intermediate fluid, would allow to

increase energy efficiency, without having release of radionuclides inside the power cycle.

Figure 2 shows the scheme of a conventional loop for the transfer of heat from the core to the power cycle, inside an LMFBR reactor [7]. As can be seen in the figure, it is possible to remove the first Na-Na heat exchanger and directly transfer heat to the secondary fluid, in this case steam, through an AIHX heat exchanger ("Advanced Intermediate Heat Exchanger") like the one shown in Figure 2.

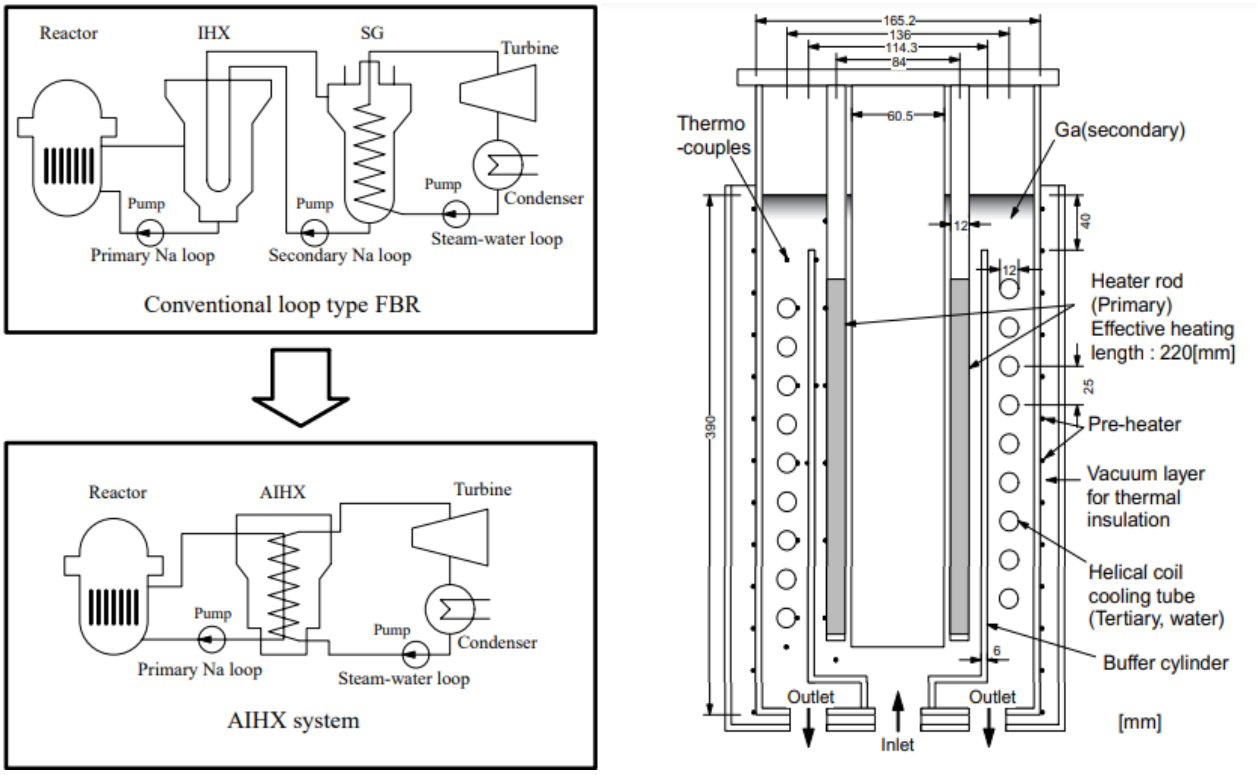

Figure 2. Elimination of the intermediate loop (on the left) in a LMFBR reactor and scheme of an experimental setup of the heat exchanger (on the right) [7].

The heater rod supplies the heat (acting as primary fluid) which is transferred to the external coils containing water (secondary fluid) through an intermediate medium, as gallium. In the case of failure and release of radionuclides, these would not enter the power cycle but would be removed with the flow of gallium. Furthermore, if air were used as secondary fluid instead of water, it would be even more difficult for tritium to enter the power cycle as it would react with oxygen forming a vapor layer that would act as a barrier for the diffusion of further tritium.

2.2.2. Double wall heat exchanger

Double-wall exchangers are a technology that has been used for several years for the heat exchange between very reactive fluids. The idea behind this design is to separate the two fluids with an intermediate layer filled with a gas with high thermal conductivity (e.g. helium), which allows heat transfer between the primary and secondary fluid, and at the same time chemically separates them.

In fusion reactors, if there is a failure of the heat exchanger wall, tritium diffusion into the intermediate layer would occur. In this case the addition of a small amount of oxygen in the intermediate layer would lead to the formation of a thin layer of vapor, thanks to the oxidation of the tritium, which would not diffuse through the metal walls of the heat exchanger. This oxide layer would act as a barrier against the permeation of the tritium itself from the FLiBe to the intermediate zone.

Due to the relatively low thermal conductivity of FLiBe compared to other molten salts, the optimal design would be a fluted tube with an annular region for the passage of the intermediate gas [4].

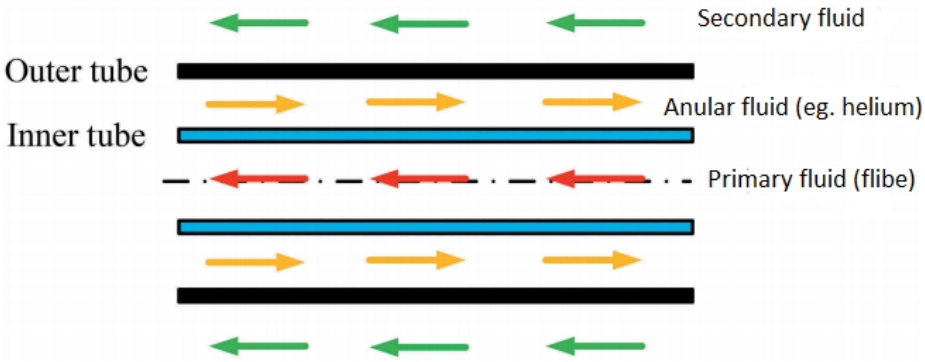

Figure 3. Design concept of a tubular double wall heat exchanger [4].

2.2.3. Heat pipes

The latest technology considered for heat removal in the ARC reactor are heat pipes.Heat pipes are a technology used for decades in different applications (e.g. for cooling electronic devices, space applications, solar thermal power, passive removal in fission reactors), as they offer several advantages over other technologies, such as the possibility to work passively or to regulate the temperature and the power exchanged.
In the context of the ARC reactor, the heat pipes technology would bring in the following advantages:

- the possibility of removing tritium;
- the possibility of controlling the temperature and avoiding the dispersion of heat (and the consequent freezing of FLiBe) when the reactor is switched off;
- they allow to isolate two environments at different pressures, such as molten salts and air, as well as chemically separate them.

These aspects will be further explored in the next chapter.

3. Heat pipes: technology and operating limits

As previously mentioned, heat pipes have been studied for decades for heat transfer, therefore they have undergone numerous improvements and design changes over time [8]. There are different types of heat pipes for numerous fields of application, differing from each other in geometry, heat transfer fluid and many other aspects.

3.1. Technology description

Despite the numerous designs proposed over the years and the improvements made on them, all heat pipes are based on the same operating principle, represented in Figure 4 ([9]). The figure shows the basic scheme of a cylindrical heat pipe: a heat transfer fluid (e.g. water) is placed inside a pipe where the vacuum has been created and then sealed. At the ends of the tube there are the heat source (evaporator) and the heat sink (condenser). The fluid undergoes phase transitions inside the tube flowing in two different regions: the vapor phase will flow inside the inner part of the tube while the liquid will flow in the annular region. The evaporator supplies the heat necessary for the evaporation of the fluid, causing an increase in pressure which will lead the vapor to move towards the condenser, where it will be returned to the liquid state, passing through a porous medium (wick), thanks to the capillary effect, and finally returning to the evaporation section. The intermediate region is insulated and can be approximated as adiabatic.

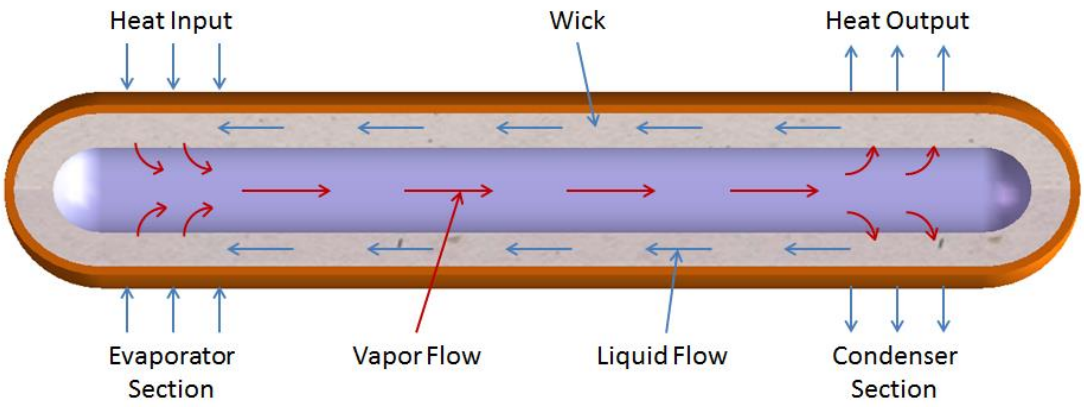

Figure 4. Basic scheme of a cylindrical heat pipe [9].

3.2. Choice of materials and heat transfer fluid

In this paragraph the fluid and the materials to be used for the construction of the heat pipe will be identified. In order to make the heat pipe suitable for the application of interest, it must be able to perform a series of tasks, such as withstanding the high temperatures involved, avoiding the diffusion of tritium into the secondary fluid, and presenting a high resistance to corrosion.

3.2.1. Heat transfer fluid

The choice of fluid is strictly linked to the temperature range in which the fluid should work. The fluid must have sufficiently high vapor pressure at temperature above the melting point of the FLiBe, in order to be able to move the vapor from one part of the tube to the other. Figure 5 shows the vapor pressures of four candidate fluids: sodium, potassium, lithium and cesium. From the pressure curves it is possible to establish the temperature ranges of use, summarized in Table 2.

Table 2. Operating temperatures range and boiling point of the four candidate fluids.

	Boiling point [K] at 1 atm	**Operating range [K]**
Lithium	1403	1100-1400
Sodium	1156	873-1100
Potassium	1032	600-800
Cesium	944	550-740

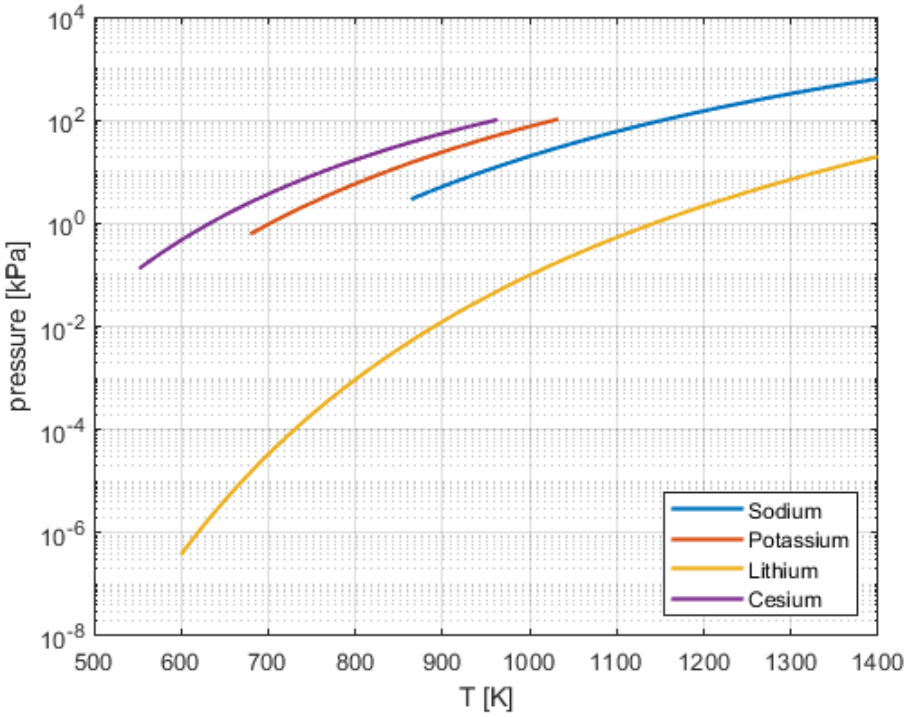

Figure 5. Vapor pressures of sodium, potassium, lithium and cesium.

As we can see from the graph the only fluids capable of working below the FLiBe melting temperature are potassium and cesium, which have sufficiently high pressures (of the order of kilopascals) to move the vapor across the tube and exchange significant heat. Lithium begins to have the same order of magnitude of vapor pressure (kilopascals) above 1100 K, therefore it is not particularly suitable for the application analyzed in this work. The last option is sodium, which begins to have acceptable values of pressure above 800 K, therefore exactly matching the range of temperatures of the salts. On the other hand, sodium has relatively low pressures below the melting temperature of the salts, which makes it perfect for this application, since in the event of shutdown of the reactor the temperature of the salts would drop causing a decrease in pressure inside the heat pipe which would lead to a practically zero heat exchange, avoiding the freezing of the FLiBe. This peculiarity of the heat pipes can be further highlighted by adding a non-condensable gas inside the heat pipe (VCHP - "Variable Conductance Heat Pipe") (Figure 6). The non-condensable gas, with a lower density than sodium, would in fact be 'crushed' at the end of the tube during normal operation. When the temperature inside the tube begins to drop, the sodium pressure (which is in saturation conditions) will drop accordingly and the inert gas will therefore be able

to occupy an increasingly larger portion of the tube, until it covers the entire condenser, hindering heat removal and avoiding freezing of salts.

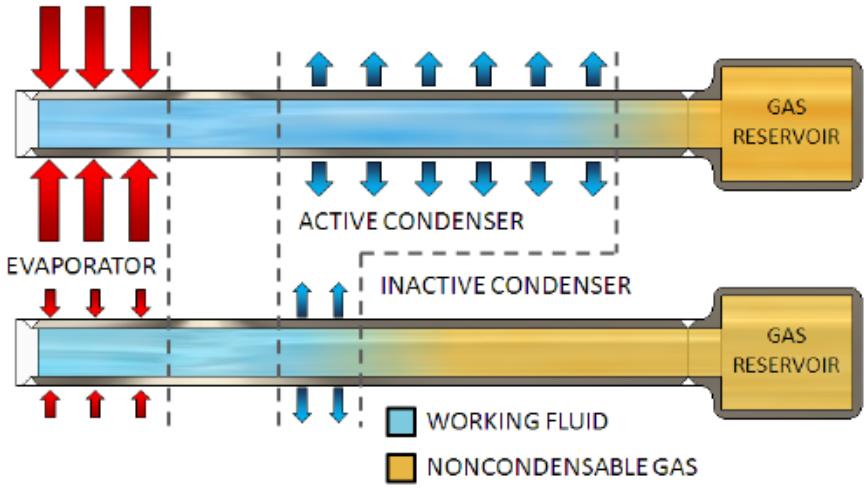

Figure 6. Variable Conductance Heat Pipe (VCHP) operating principle [10].

For each fluid a Merit number N_l can be defined, which describes its performance:

$$N_l = \frac{\rho_l \lambda_{fg} \sigma}{\mu_l} \tag{1}$$

where:

- ρ_l is the liquid density of the fluid;
- λ_{fg} is the latent heat;
- σ is the surface tension;
- μ_l is the dynamic viscosity of the liquid.

The fluids with high latent heat of vaporization are able to exchange greater power with the same flow. At the same time high liquid density and surface tensions will allow to achieve a greater pumping capability, while low viscosity will lead to lower pressure drop inside the wick. In Figure 7 are shown the merit number for various fluid commonly used in heat pipes, as it possible to notice sodium has the highest merit number, which further explains the reason of its choice [11].

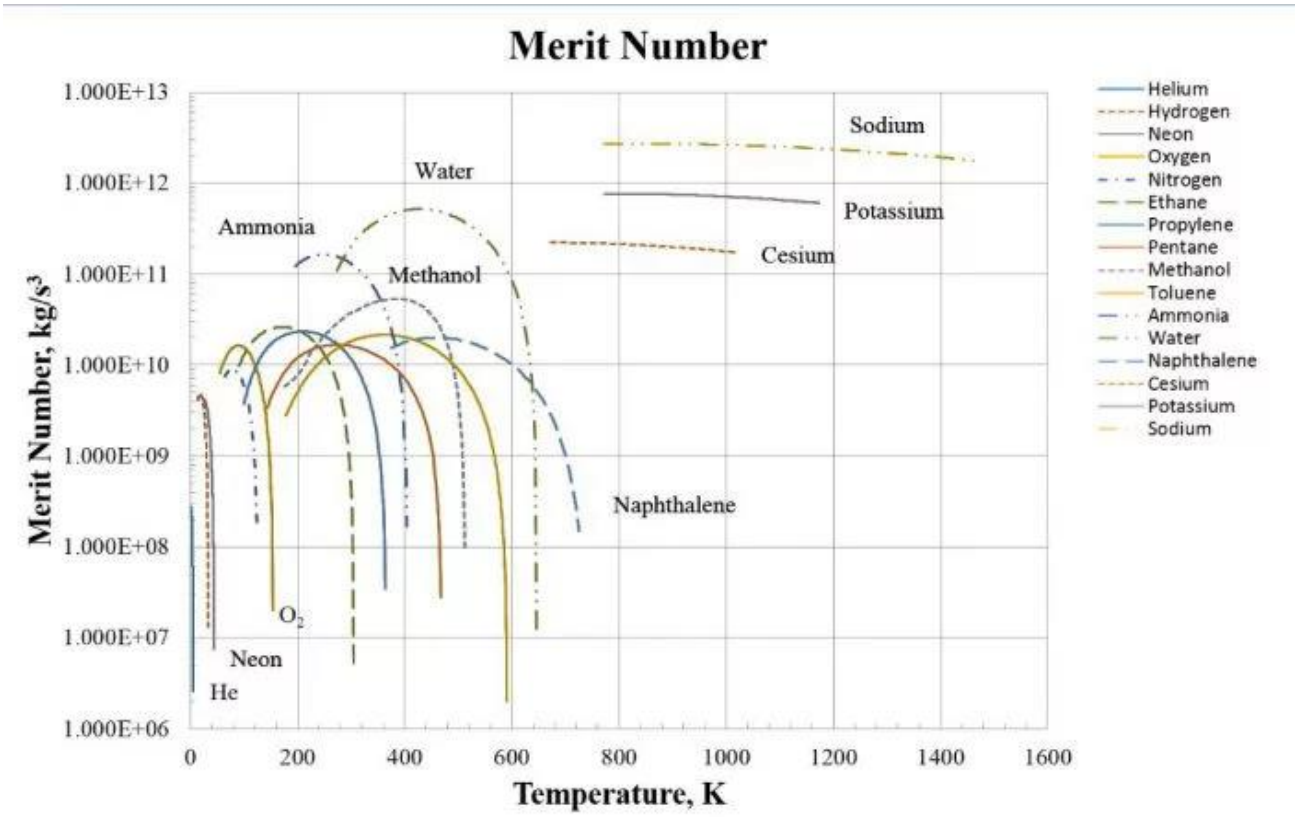

Figure 7. Merit number for different working fluids [11].

3.2.2. Porous matrix

The wick provides a means for the liquid to return to the evaporator. The wick structure must be well dimensioned, providing enough liquid to the evaporator in order to avoid dry-out and overheating of the heat pipe, resulting in failure. This eventuality must be analyzed in the design phase, through the capillary limit, which will be considered in the dedicated chapter. There are three types of wick structures, shown in Figure 8 [12]:

- Grooved wicks:

Grooved wicks are essentially shallow grooves on the inner surface of the heat pipe. Their cross section shape can be triangular or rectangular but the most used are trapezoidal. The liquid passage channels are much larger with respect to the other types, resulting in a low capillary effect but also with the lowest pressure drops.

- Screen wicks

Screen wicks are woven meshes made up of several metal wires wrapped around the tube. The area of the regions where the liquid passes depends on the mesh size, i.e. the number of woven wires, but in any case it is smaller than the size of the pores obtained with the sintering process. This results in lower capillary action and generally lower performance with respect to sintered wicks but they are also much less expensive.

- Sintered wicks:

Sintered wicks are made from very fine metal powders which are then heated to high temperatures. At a temperature close to 80% of their melting temperature they begin to sinter forming a porous medium. The size of the pores and their shape depends on the sintering process as well as on the material used, but in many cases for the analytical analysis of the wick structure the pores can be considered spherical. The pores size obtained through sintering is lower with respect to the other types of wick, which also means greater pumping capability. The sintering process is obviously much more expensive than the other methods seen above.

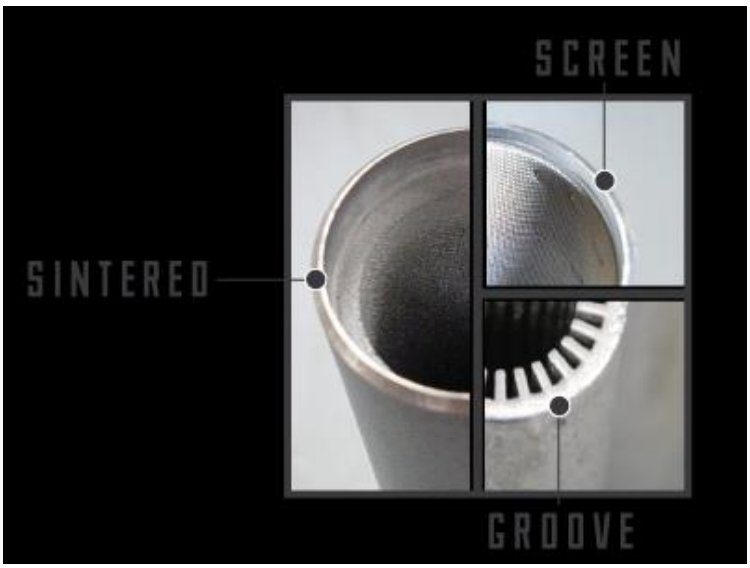

Figure 8. Different type of wicks [12].

There are several properties that describe the quality of a wick and often their determination is not trivial. The main properties of the wick are certainly porosity, permeability, and effective pore radius, which are briefly described below:

- **Porosity:**

The porosity is calculated as the ratio of total pore volume to total volume (pores plus solid structure). The porosity of the wick can vary from 40% (average value for a sintered wick) to 70-80%.

- **Permeability:**

Permeability is an index of the ease with which the liquid passes through the pores. For single phase flow, it can be predicted through Darcy's law, according to which the flow is directly proportional to the pressure drop and inversely proportional to the viscosity of the liquid at low velocity regimes.
In some cases, however, Darcy's law could lead to non-negligible errors in the calculation of permeability, in these cases other equations are used, such as that of Kozeny-Carman, which describes the flow through a packed bed:

$$K = \frac{\varepsilon^2 d_w^2}{C*(1-\varepsilon)^2} \quad [m^2] \tag{2}$$

Where:

- ε is the porosity of the wick;
- d_w is the the wire diameters (in the case of screen mesh);
- C is a geometrical factor depending on the properties of the wick structure. For a uniformly packed structure, the common values of C are 122,150 or 180.

- **Pores size:**

The pore size plays a fundamental role in the quality of the wick: the smaller the surface of the pores, the higher the pumping capability. The best values of the pores size are obtained with the sintering process (10-100 μm). It is not always easy to determine the pore size of a wick, especially for sintered ones, due to the different size and shape of the pores inside the porous 3D matrix.

The wick chosen for this study is a screen mesh type made up using 100 wires of SS304 per inch, with a diameter of 0.09 mm each [13]. The choice to use a screen mesh wick instead of a sintered one comes from the fact that for the application of interest in this study, a large number of heat pipes will be needed, and the cost would be much higher. The wick has been found to have a porosity and permeability of 70% and $2.76*10^{-10}$ respectively [13].

The optimal situation for a wick is to have small pore sizes (i.e. high pumping capability) together with high permeability (i.e. lower pressure drops). Unfortunately, these two properties are mutually exclusive, as permeability increases as the radius of the pores increases. It is necessary therefore to find a trade-off between these two properties. In Figure 9 is shown the relationship between the pore radius and the permeability for different materials, obtained with the Anderson curve [14]:

$$K = 0.125 * r_c^{2.207} \ [\text{m}^2]$$

where r_c is the pore size in [m].

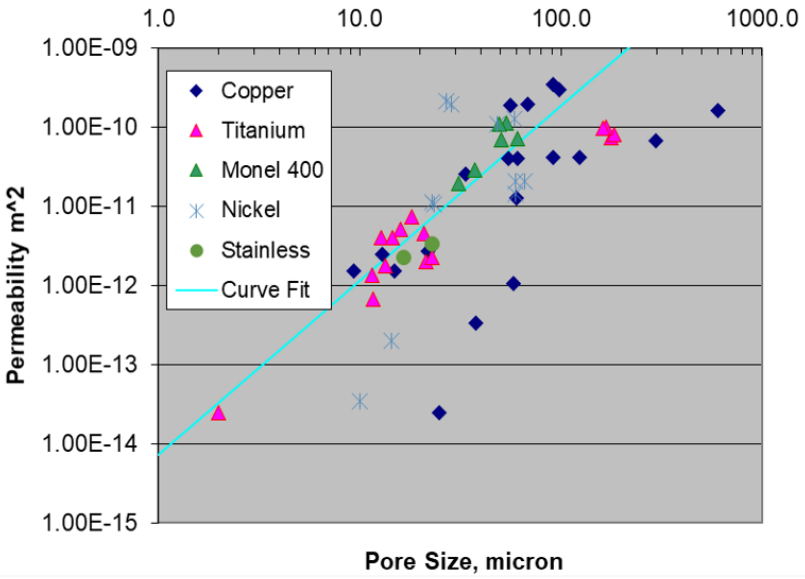

Figure 9. Relationship between pore size and permeability [14].

In order to fully define the properties of the wick, it is also necessary to use a thermal conductivity value that takes into account the presence of pores and liquid with respect to bulk SS304. It is therefore used a conductivity value, called effective thermal conductivity, which considers all these factors. The effective thermal

conductivity for the wick in question was calculated as an average over the total volume, which represents solid and fluid stripes in parallel to the heat flux:

$$k_{eff} = \theta_s K_s + \theta_f K_f + K_{disp} \quad (3)$$

where:

- $\theta_{s,f}$ and $K_{s,f}$ are the volume fractions and the thermal conductivity of the solid and the fluid respectively;
- K_{disp} is an additional term due to the microstructure of the pores. In fact, the liquid will follow a swirled flow inside at the pore scale, resulting in an heat exchange enhancement.

The value of k_{eff} obtained with this approach is 48.462 W/(m·K).

3.2.3. External wall

The external walls of the heat pipe have to comply with some requests. They must be thick enough to withstand the drag force imposed by the forced convection on the external surface by the FLiBe and the secondary fluid flows, and they must have good thermal conductivity to effectively transmit heat in the evaporator and condenser area. They must also be resistant to corrosion and finally it would be preferable that they were also impermeable to tritium, as will be discussed in Chapter 4. The material chosen for the external wall is therefore Hastelloy®N, a nickel base alloy with good oxidation resistance to hot fluoride salts. The chemical composition of Hastelloy®N is resumed in Table 3, together with its thermal properties of the alloy, which were assumed constant [15].

Table 3. Chemical composition and thermal properties of Hastelloy®N [15].

Weight [%]	
Nickel	71
Molybdenum	16
Chromium	7
Iron	5 max.
Silicon	1 max.
Manganese	0,8 max.
Carbon	0,08 max.
Cobalt	0,2 max.
Copper	0,35 max.
Tungsten	0,5 max.
Aluminum+Titanium	0,5 max.
Thermal properties	
Density [kg/m³]	8860
Thermal conductivity [W/(m*K)]	11,5
Heat capacity at constant pressure [J/(kgK)]	570

3.2.3.1. The problem of corrosion

Although Hastelloy®N promises excellent corrosion resistance, after several hours of immersion there will be some weight losses near the surface, which could be not negligible. Recent studies on the corrosion effect of Hastelloy®N immersed in FLiNaK salts confirm this last consideration [16]. Figure 10 shows the weight loss for an immersion time of 1000 hours. As it possible to see from the graph, during the first 100 hours of immersion the weight loss is very high and then decrease in the following hours. The most reactive components of Hastelloy®N, which contribute mostly to corrosion, are Cr and Mo, and their depletion on the exposed surface after the first 100 hours justifies the decrease of the corrosion phenomenon.

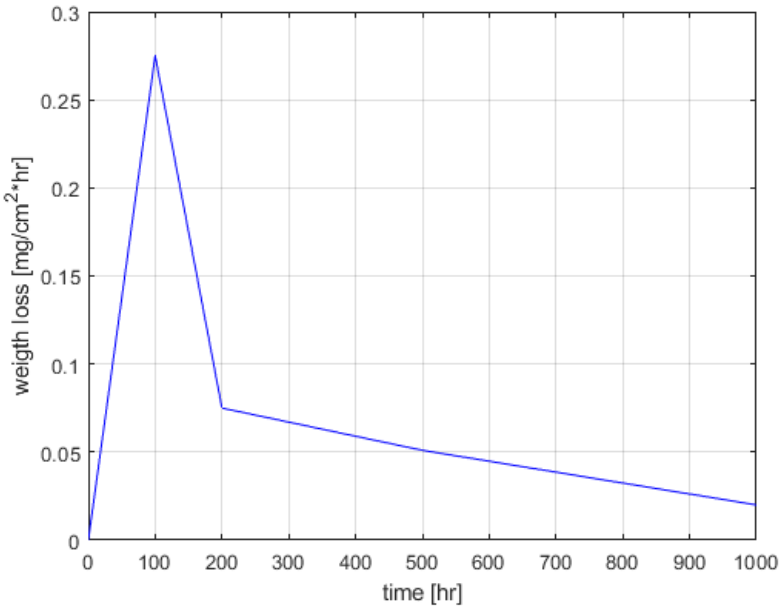

Figure 10. Corrosion rate of Hastelloy®N versus immersion time in FLiNaK salts. The samples were examinated at 100,200,500,1000 hours [16].

From the plot above is possible to find the surface thickness of the Hastelloy®N consumed after 1000 hours of immersion. Integrating the curve of weight loss in fact it is possible to find the superficial weight loss (in kg/m^2) and then dividing that value for the density of the Hastelloy®N it is possible to find the thickness reduction after 1000 hours. The value of the consumed thickness found is equal to 76.64 µm after 1000 hours of immersion. The value obtained can't be neglected, especially considering that in the study used as a reference, the corrosion was studied as result of the simple natural convection of salts, while in this study the heat pipe would be subject to an external flow of salts with a certain speed, certainly resulting in a greater weight loss for equal hours of operation. To better understand the entity, if an external wall with a thickness equal to 2.5 mm were used, after 1000 hours of operation there would be a reduction of the thickness of about 3%. Fortunately, the problem can be solved quite easily through a very thin layer (some microns) of sligthly sensitive to the phenomenon of corrosion (e.g. tungsten), which brings also the double advantage of being impermeable to tritium.

3.3. Operational limits

The limiting criteria for the design of the heat pipes is the heat power exchanged from the evaporator to the condenser, which could lead to several undesirable phenomena if it exceeds some operational limits. These limits are due to different physical phenomena, and only some of them play a relevant role for the application under examination, which are summarized below:

- **Entrainment limit**

The steam flow exerts shear stresses on the porous wall inside which the liquid flows. At sufficiently high speeds some droplets of liquid can be transported by the vapor and return to the condenser, worsening the performance of the heat pipe. The maximum value of the heat transfer rate, in order to avoid the entrainment, is calculated as follows:

$$Q_{entr}\ [W] = A_{vap} * h_{fg}(T) * \sqrt{\frac{\rho_v(T)*\sigma(T)}{2*r_{eff}}} \quad (4)$$

where:

- A_{vap} is the cross section of the vapor core [m^2];
- $h_{fg}(T)$ is the latent heat of sodium [J/kg];
- $\rho_v(T)$ is the vapor density of sodium [kg/m^3];
- σ is the surface tension of sodium [n/m];
- r_{eff} [m] is the effective pore radius, which was calculated as $r_{eff} = \frac{d+w}{2}$ where d is the diameter of the fibers of the wick, and w is the distance between the fibers.

- **Capillary limit**

The capillary pressure that a heat pipe is able to develop is equal to:

$$\Delta \mathrm{p_c} = \frac{2\sigma(T)}{r_{eff}} \tag{5}$$

where "r_{eff}" is the effective pore radius. The capillary limit is reached when the capillary pressure equals the pressure drops that occurs inside the pipe. These are drops due to vapor flow ($\Delta \mathrm{p}_V$), the drops due to gravity ($\Delta \mathrm{p}_g$), and the ones needed to drive the liquid through the wick ($\Delta \mathrm{p}_l$):

$$\Delta \mathrm{p}_C = \Delta \mathrm{p}_V + \Delta \mathrm{p}_g + \Delta \mathrm{p}_l \tag{6}$$

The gravity term will be counted with the opposite sign compared to the other pressure drops if the heat pipe is arranged vertically with the evaporator in the lower part. In this case the liquid will be pushed by gravity, explaining why it's convenient to place the heat pipe vertically. The liquid term can be obtained from Darcy's law as follow:

$$\Delta \mathrm{p}_l = \frac{L_{eff}\mu_l(\mathrm{T})\mathrm{V}}{KA_w} \tag{7}$$

where:

- A_w is the cross section of the wick [m^2];
- K is the permeability of the wick [N/m];
- $\mu_l(T)$ is the liquid viscosity [Pa∗s];
- L_{eff} is the effective length of the heat pipe, calculated as $L_{eff} = 0.5 * (L_{eva} + L_{cond}) + L_{ad}$, where L_{eva},L_{cond} are the lengths of the evaporator and the condenser and L_{ad} is the length of the adiabatic section.
- V is the volumetric flow rate [m^3/s], which can be calculated as:

$$V = \frac{Q}{\rho_l(T)h_{fg}(T)} \tag{8}$$

While the gravity term can be calculated as:

$$\Delta p_g = -\rho_l(T)\, g\, L_{eff} \tag{9}$$

Substituting eq. (8) in eq. (7) and then replacing the resulting expression in eq. (5) together with equation (6) and (9), and neglecting the vapor term, the following expression is obtained:

$$Q_{cap}\ [W] = \frac{K\ \rho_l(T)\ A_w\ h_{fg}(T)}{\mu_l(T)\, L_{eff}} * \left(\frac{2\sigma(T)}{reff} + \rho_l(T) * g * L_{eff}\right) \tag{10}$$

- **Sonic limit**

When the temperature inside the tube decreases the vapor pressure drops, in order to transfer a given amount of heat the velocity of the vapor will increase, and also the pressure drop between the evaporator and the condenser will increase. When the vapor at the end of the evaporator section (i.e. at the beginning of the adiabatic zone) reaches the speed of sound the sonic limit is reached, with important flow compressibility effects. The sonic limit is therefore reached when there are high powers at low temperatures, and consequently will occur mainly during the start-up of the heat pipe and will self-correct.

$$Q_{sonic}\ [W] = A_{vap}\, \rho_v(T) h_{fg}(T) \frac{v_s(T)}{\sqrt{2(\Upsilon(T)+1)}} \tag{11}$$

where:

- $v_s(T)$ is the speed of sound [m/s];
- ρ_v(T) is the vapor density [kg/m^3];
- $\Upsilon(T)$ is the ratio of specific heats.

The power limits with which the heat pipe will have to work will be the minimum of all limits at any temperature. In order to take into account possible manufacturing defects, it was decided to assign a safety factor of 0.75 to the entrainment and capillary limits, and a safety factor of 0.5 for the sonic limit:

$$Q_{max} = \min(0.75 * Q_{entr}, 0.75 * Q_{cap}, 0.5 * Q_{sonic})$$

The operating limits of a 4 m long sodium heat pipe, with an external diameter of 3 cm, are shown in Figure 11. The area below the black dotted line is the operating area of the heat pipe, which is limited for the temperature range 800-940 K by the entrainment limit while for higher temperatures the limit to be taken into consideration is the capillary one. The most immediate solution to increase the entrainment limit is to increase the radius of the vapor cavity, thus increasing A_{vap} in equation (4), while increasing the thickness of the wick (thus increasing term A_w in equation (10)) leads to an improvement of the capillary limit. These considerations will be taken up later in chapter 5.5.4.1.

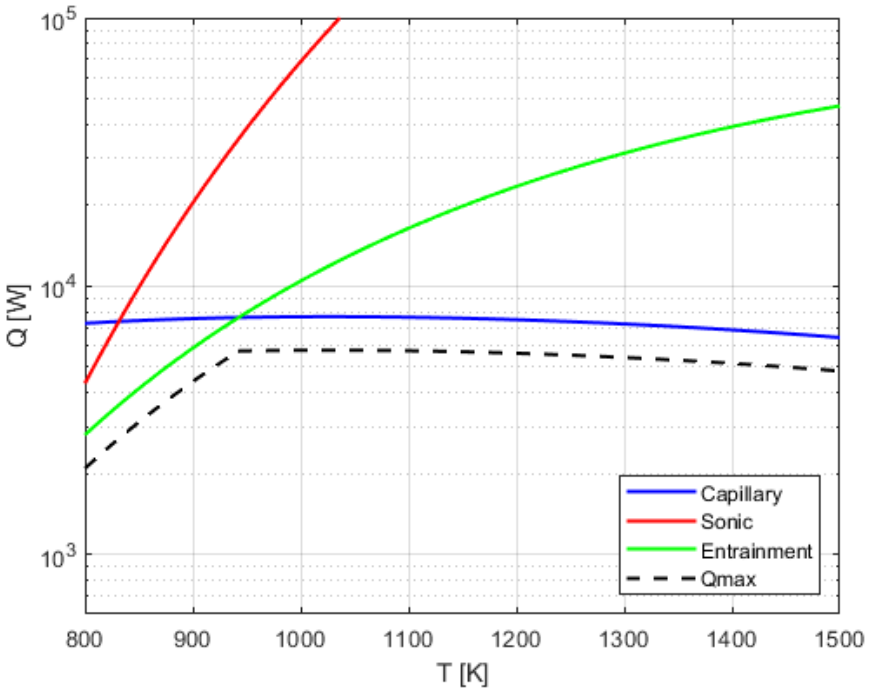

Figure 11. Heat pipe limits vs evaporator exit temperature for a 4 m long pipe and 3 cm outer diameter (wick thickness = 3 mm, external wall thickness = 2,5 mm).

4. Heat pipes heat exchanger

Inside the reactor huge quantities of thermal power are transferred to the salts: about 630 MW of thermal power is expected to be provided to bring the salts to the outlet temperature of 880 K. This is more or less the power that the heat exchanger must be able to exchange to bring back the salts to 800 K. In order to exchange such high powers, a considerable amount of heat pipes in series will undoubtedly be needed. Figure 12 shows the general scheme of the heat exchanger: it consists of several rows of heat pipes arranged vertically with the evaporators in the lower part of the exchanger and the condensers on the upper part. The pipes will be subject to forced convention of the two fluids of interest, namely the FLiBe in the lower part and a secondary fluid in the upper part (eg. helium, air), whose choice will be discussed in paragraph 4.1.

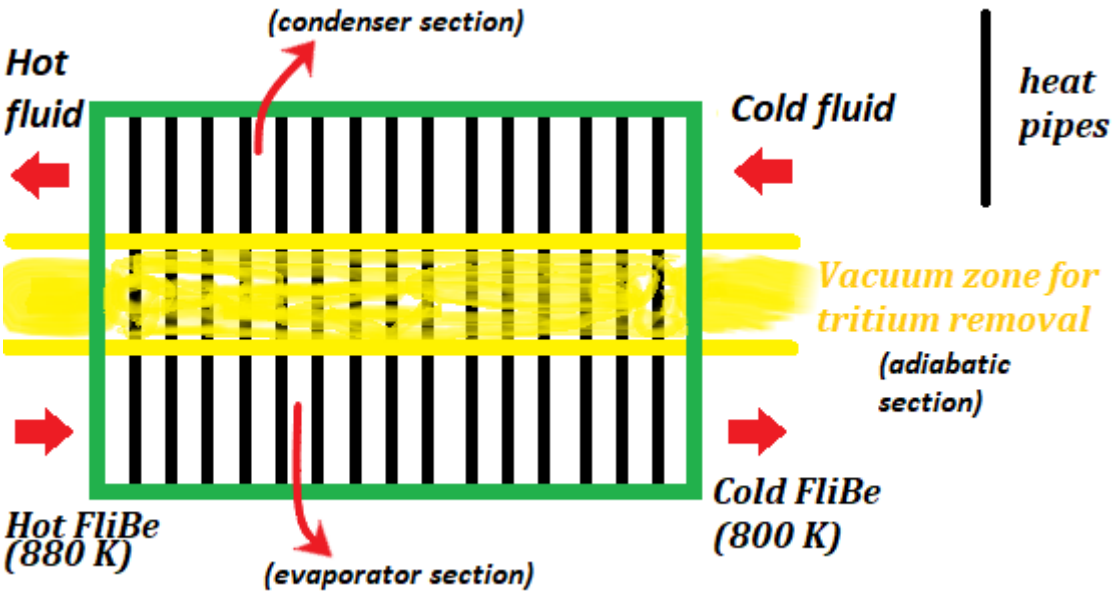

Figure 12. Scheme of the heat pipe heat exchanger.

The heat pipe heat exchanger shown in Figure 12 offers several opportunities of great interest for the application analyzed. As anticipated in chapter 2.2.3 one of the greatest advantages, besides the chemical and physical separation of the secondary fluid from the salts and the avoidance of the freezing of the salts, is the possibility of removing the tritium. In the adiabatic regions of the heat pipes, part of the tritium present in the molten salts can be eliminated through tritium-permeable

materials (e.g. nickel), imposing a depression on the outside of the pipes in that region, thus 'forcing' the tritium to cross the walls of the heat pipe and be removed. The use of a thin layer of anti-corrosion material (i.e. tungsten), which is at the same time impermeable to tritium, allows to create a double barrier for the removal of tritium. In fact, if small quantities of tritium were able to pass through the walls of the tube to the evaporator, they would in any case be removed in the adiabatic part, as described above.

4.1. Choice of the secondary fluid and power cycle

The choice of the secondary fluid and the power cycle is fundamental to exploit the power produced inside the reactor in the best possible way. There are several recent studies [5] that analyzed the possibility of implementing a Rankine cycle for the production of electricity. Despite the interesting results, the Brayton cycle is still believed to be the best option, matching better with the temperatures of the ARC reactor. Two different fluids to be used inside the reactor were considered: air and helium. Air would certainly be the simplest choice from the point of view of system design, as it has been used for decades in Brayton cycles. On the other side helium brings some advantages from the point of view of thermodynamic performance, but certainly with greater complexity in the design due to the higher pressures involved. Another interesting option is supercritical CO_2, which guarantees the best thermodynamic efficiency and compactness of the plant (as recent studies suggest [5]) for turbine inlet pressures close to 250 bar, which is the technical limit set for the state of the art technology. It was decided not to consider supercritical CO_2 as a possible fluid, since the cross flow at such high pressures on the secondary side of the pipes, which have a diameter of a few centimeters each and a wall thickness of a few millimeters, would lead to high mechanical stresses, causing safety problems inside the heat exchanger. The scheme of the Brayton cycle is shown in Figure 13: as it possible to see some variations have been made with respect to the basic Brayton system [5]. A heat recovery unit (REC) has been added in order to recover the heat from the helium exiting the turbines, which is hundreds of kelvins above the room temperature. The second improvement consists into splitting the compression in two separate stages, adding an intercooler (IC) in the middle: this allows to reduce the irreversibility generated during the

compression phase, caused by the change in density due to the increase in temperature. The last modification, with respect to the simple Brayton cycle, consists in adding another heat exchanger (RE) between the two turbines in such a way as to increase the enthalpy jump at the extremes of the second turbine, and consequently the power produced. There are other modifications to the system that could be made, for istance adding other compression/expansion steps, or combining the Brayton cycle with a Rankine cycle, but they are beyond the scope of this thesis.

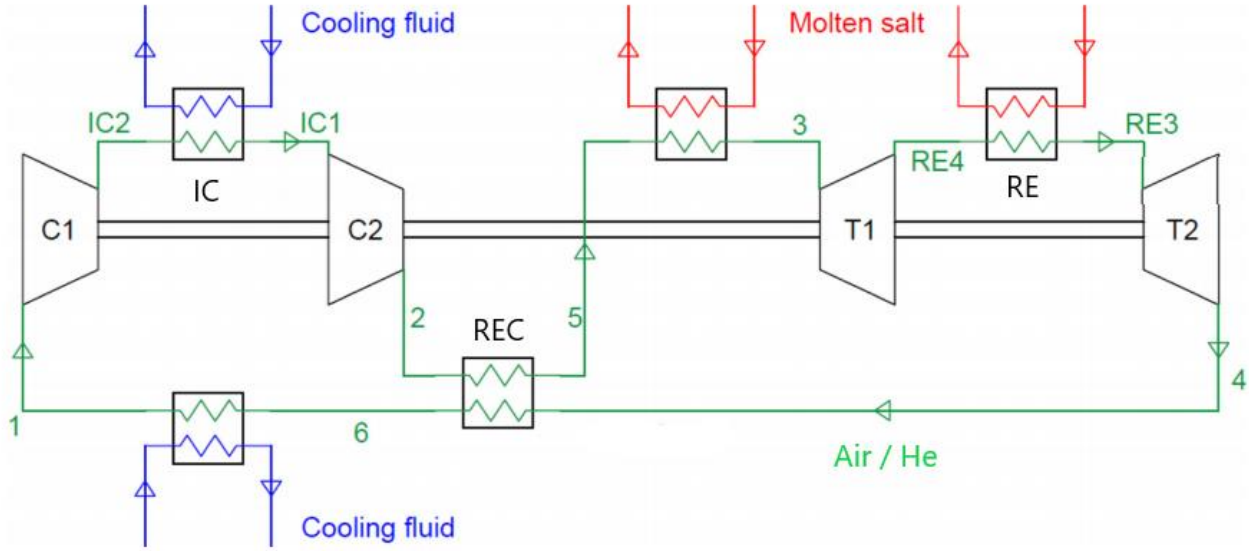

Figure 13. Scheme of the Brayton cycle with IC, RE, REC [5].

For the numerical analysis carried out in the next paragraph, only the molten salt heat exchanger placed before the first turbine was considered. The values summarized in Table 4 were used as inlet pressure and velocities in the heat exchanger: for helium a pressure of 25 bar was considered, as a value that guarantees the best thermodynamic efficiency of the cycle [5], while for the air was assumed a compression ratio equal to 10, with pressure p_1 equal to the ambient pressure.

Table 4. Inlet pressure and velocities for air and helium.

	Heat exchanger inlet conditions	
	Air	**Helium**
Velocity [m/s]	10	10
Pressure [bar]	10	25

5. Numerical analysis

In this part of the study a stationary analysis of a single heat pipe subjected to the thermal loads provided in the application of interest is carried out. The Comsol Multiphysics software was used for the computational calculation.

5.1. Geometry and mesh definition

The model analyzed is a vertically arranged cylindrical heat pipe that uses sodium as fluid. The condensation area is placed in the upper part of the tube while the evaporator is located in the lower part. The tube is closed at both ends by two hemispherical caps. The internal surface of the tube is entirely covered by the wick, inside which the liquid sodium passes. The heat pipe analyzed in this study has a length of 4 m, according to [10], and an external diameter of 53 mm, with a thickness of the outer wall equal to 2.5 mm along the evaporator/condenser sections and equal to 1 mm in the adiabatic section, while the thickness of the wick is equal to 2 mm. The length of the evaporator/condenser sections is equal to 1.5 m. The geometry adopted in Comsol Multiphysiscs for this first stationary analysis is shown in Figure 14: in order to make the geometry more visible, the lengths of the heat pipe in figure has been reduced by a factor of 30, keeping the thicknesses of the walls fixed.

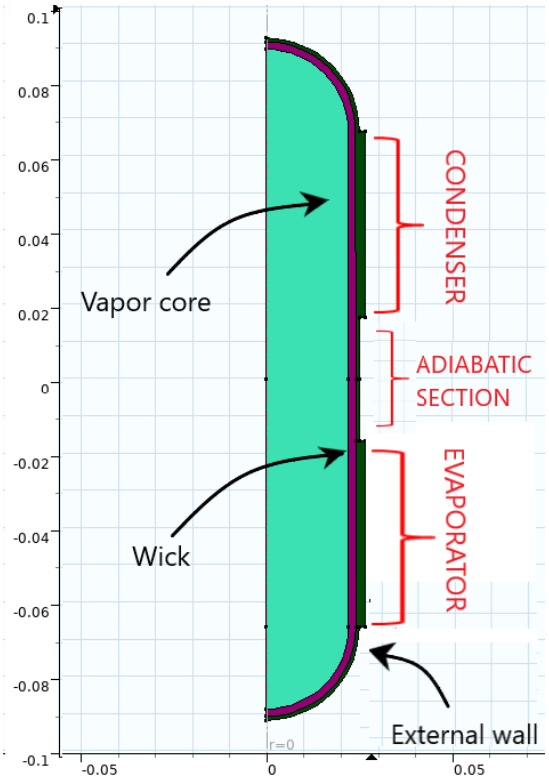

Figure 14. Geometry of the heat pipe used in Comsol Multiphysics.

For the definition of the mesh, two different distributions for the condenser/evaporator sections and for the adiabatic section have been considered, as shown in Figure 15. In the regions subjected to forced convection (i.e. condenser and evaporator), higher temperature gradients are expected within the vapor core. Therefore, the flow of sodium vapor in these regions will undergo changes in direction passing from vapor to liquid or vice versa and entering/exiting inside the wick, resulting in higher velocity gradients with respect to the adiabatic region of the pipe. For these reasons it was decided to apply a square mesh in the central region, for an axial length equal to:

$$L = L_{ad} - 2 * 0.05 * L_{eva}$$

where:

- L_{ad} is the length of the adiabatic region [m];
- L_{eva} is the length of the evaporator/condenser [m].

In this way the square mesh extends up to just before the condenser/evaporator, as that area is already strongly affected by the effects mentioned above, with high

temperature and velocity gradients of the vapor. Therefore 150 meshing elements were used for the central area, while for the evaporation/condensation sections a triangular mesh was used with maximum and minimum allowed values of the element size equal to 2.5 mm and 1 mm, respectively. From Figure 15 it is also possible to notice that the mesh becomes finer near the liquid-vapor interface. This is due to the fact that the condensation/evaporation of the vapor/liquid particles occurs in that region. Thus, it was chosen to adopt 8 additional boundary layers in this region, with a stretching factor equal to 1.2 (i.e. between two subsequent boundary layers the dimensions increase by 20%).

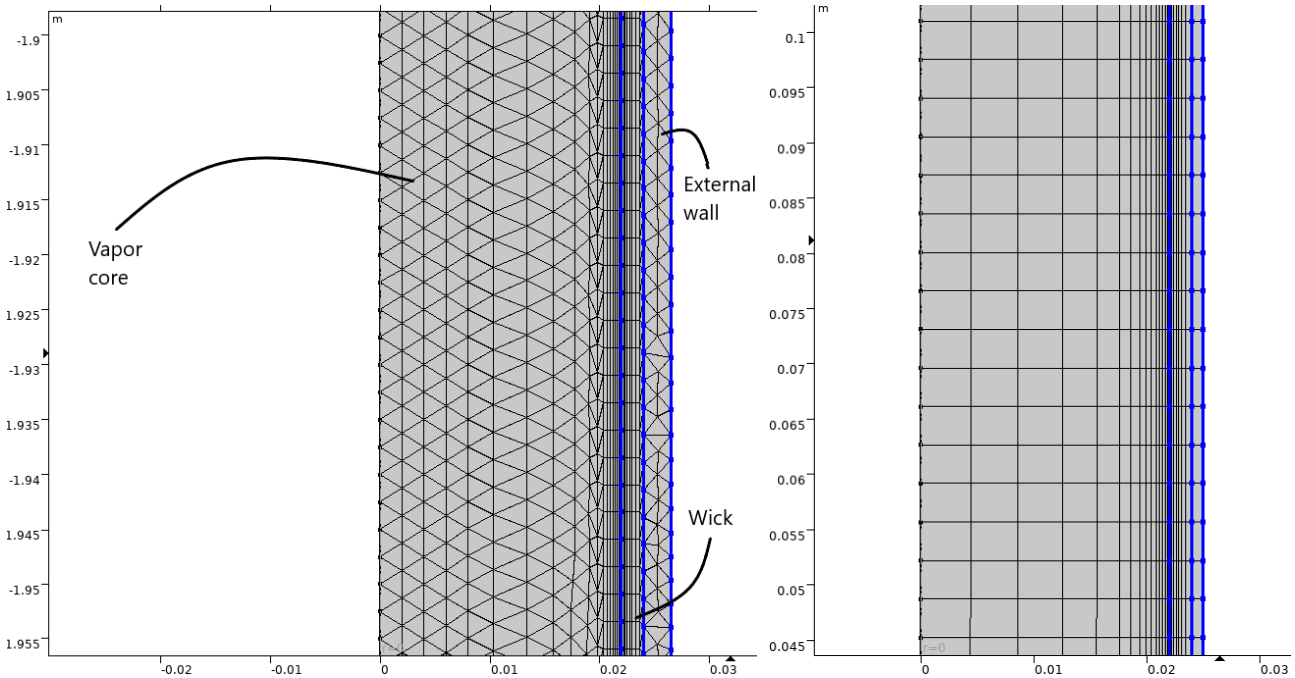

Figure 15. Mesh adopted for the evaporator/condenser sections (on the left) and for the adiabatic region (on the right).

5.2. Equations and boundary conditions

In the following pages the equations and boundary conditions used within the Comsol Multiphysics model for the computation of the velocity fields, pressure and temperature inside the model will be illustrated.

5.2.1. Fluid flow problem

5.2.1.1. Vapor cavity

The vapor flow in the inner region of the heat pipe can be assumed laminar. The Navier-Stokes equation are the used to compute the pressure and velocity field:

$$\rho\vec{u}\cdot\nabla\vec{u} = -\nabla \mathrm{p} + \nabla\cdot\left[\mu(\nabla\vec{\mathrm{u}} + (\nabla\vec{\mathrm{u}})^T) - \frac{2}{3}\mu(\nabla\cdot\vec{\mathrm{u}})I\right] \qquad (12)$$

where:

- $\vec{u}$ [m/s] is the velocity vector;
- ρ [kg/m^3] is the density of the sodium vapor;
- p [Pa] is the pressure;
- μ [kg/(m·s)] is the dynamic viscosity of the sodium vapor.

The vapor cavity condition is subjected only to two boundary conditions: one is the simmetry along the axial line and the other one is a pressure constraint applied on the inner surface of the wick. In particular, the pressure along this boundary is set equal to the vapor pressure of the sodium:

$$p = p_{sat}(T)$$

This means that liquid and vapor are in equilibrium along the liquid-vapor interface.

5.2.1.2. Porous medium

In order to compute the fluid velocity and pressure of the liquid sodium inside the porous matrix the Brinkman equations were used. They extend the Darcy's law, including the dissipation of the kinetic energy by viscous shear, similar to the Navier-Stokes equations. The dependent variables in the Brinkman equations are the velocity and the pressure.

The flow in porous media is governed by a combination of the continuity equation and the momentum equation, which together form the Brinkman equations, which in the stationary case can be written as:

$$\nabla \cdot (\rho \vec{u}) = 0 \tag{13}$$

$$\frac{\rho}{\varepsilon_p}\vec{u}\cdot\nabla\left(\frac{\vec{u}}{\varepsilon_p}\right) = -\nabla \mathrm{p} + \nabla\cdot\left\{\frac{1}{\varepsilon_p}\left[\mu(\nabla\vec{\mathrm{u}} + (\nabla\vec{\mathrm{u}})^T) - \frac{2}{3}\mu(\nabla\cdot\vec{\mathrm{u}})I\right]\right\} - \left(\frac{\mu}{K}\right)\vec{u} + \rho g \tag{14}$$

where:

- ε_p is the porosity;
- K [m^2] is the permeability tensor of the anisotropic porous medium. It is defined as $K = \begin{bmatrix} K_{rr} & K_{r\theta} & K_{rz} \\ K_{\theta r} & K_{\theta\theta} & K_{\theta z} \\ K_{zr} & K_{z\theta} & K_{zz} \end{bmatrix}$; where r,θ,z are respectively the radial, circumferential and axial directions of the cylindrical coordinates;
- $\vec{u}$ [m/s] is the velocity vector;
- ρ [kg/m^3] is the density of the liquid sodium;
- p [Pa] is the pressure;
- μ [kg/(m·s)] is the dynamic viscosity of the liquid sodium.

In equation (14) the inertial term $u\cdot\nabla\left(\frac{u}{\varepsilon_p}\right)$ was neglected, while the term ρg represents the gravity effect. It must be noticed that in this simulation the flow of liquid sodium is considered compressible, so it is not possible to extract the density from the divergence operator, since its derivatives are not null.

The physical properties of the fluid (i.e. density, viscosity) are defined as intrinsic volume averages that correspond to a unit volume of the pores, while the velocity is defined as the volume flow rate per unit cross section of the porous medium. In this way the properties in every point take into account the complexity of the three-dimensional structure of the porous medium and its heterogeneity, due to the presence of the pores. The boundary conditions used for the wick are the ones shown in Figure 16.

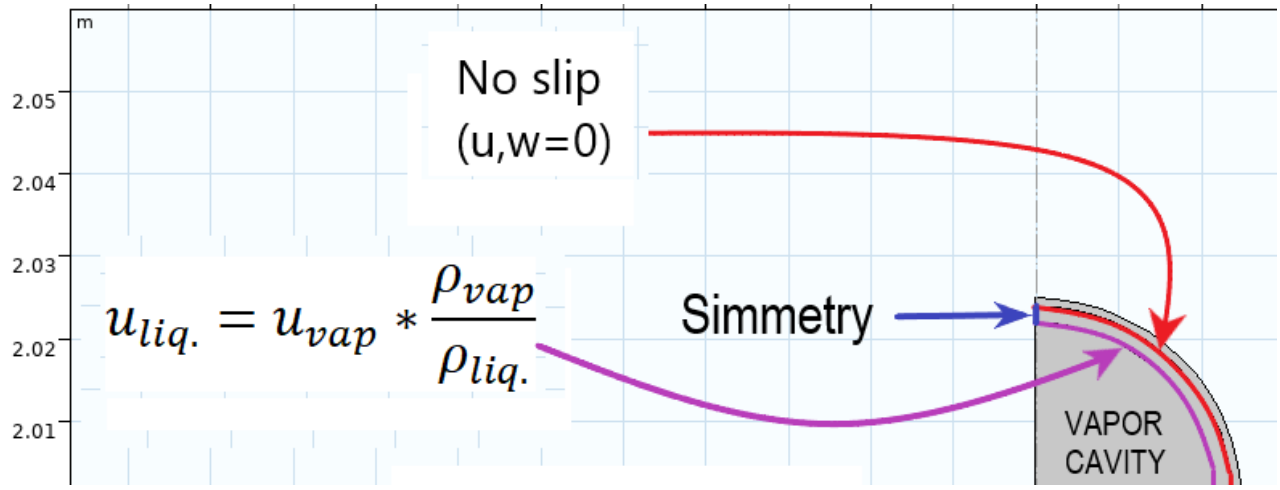

Figure 16. Fluid flow problem boundary conditions for the wick domain.

In addition to the boundary conditions in Figure 16, a point pressure limit has also been added, precisely on the external wall of the wick in the middle point of the pipe. The pressure at this point has been set equal to the sodium vapor pressure. The condition $u_{liq.} = u_{vap} * \frac{\rho_{vap}}{\rho_{liq.}}$ applied on the internal surface of the wick was derived from a simple mass conservation.

5.2.2. Heat transmission problem

The equations used for computing the temperature inside the different domains are shown below. The heat balance equation written for heat exchange in solids and fluids was used for the external wall and for the vapor respectively:

External wall: $$\nabla \cdot (q_r + q) = 0 \quad (15)$$

Vapor cavity: $$\rho c_P \vec{u} \cdot \nabla T + \nabla \cdot (q_r + q) = -\alpha T \vec{u} \cdot \nabla p + \tau : \nabla \vec{u} \quad (16)$$

where:

- q is the heat flux by exchanged by conduction, which can be written as $\mathrm{q} = k\nabla \mathrm{T}$, according to the Fourier's law [W/m^2];
- q_r is the heat flux by exchanged by radiation [W/m^2];
- α is the coefficient of thermal expansion [1/K];
- ρ is the density [kg/m^3];
- c_P is the specific heat capacity [J/(kg·K)];
- τ is the viscous stress tensor [Pa].

In order to solve the thermal problem in the wick the equations (15) and (16) were combined together, weighting the contributions of the solid and liquid phase through the volume occupied by them (i.e. through porosity):

$$\rho_f c_{P,f} \vec{u} \cdot \nabla \mathrm{T} + \nabla \cdot (k_{eff} \nabla \mathrm{T}) = -\alpha T \vec{u} \cdot \nabla \mathrm{p} + \tau : \nabla \vec{\mathrm{u}} \qquad (17)$$

Where k_{eff} is the thermal conductivity calculated with the equation (3) and $\rho_f, c_{P,f}$ are the density and specific heat of the liquid sodium.
In each point of the porous material, a local thermal equilibrium between the solid and liquid phase is imposed:

$$T = T_f = T_s$$

The boundary conditions applied to resolve the equations written above, are resumed in Figure 17. In order to take into account the latent heat released during condensation of the sodium vapor and the heat earned by the evaporation process (i.e. h_{fg}), the following boundary condition is imposed on the inner wick surface:

$$q'' = (u_{vap.}\rho_{vap.} + w_{vap.}\rho_{vap.}) \cdot h_{fg}(T) \qquad [\mathrm{W/m^2}]$$

where:

- $u_{vap.}$ is the radial velocity of the vapor at the inner wick boundary [m/s];
- $w_{vap.}$ is the axial velocity of the vapor at the inner wick boundary [m/s].

On the external wall of the heat pipe, a Robin's BC is imposed at the evaporator/condenser, using heat transfer coefficients which are found using the Churchill-Bernstein's correlation with air and FLiBe as fluids:

$$Nu_D = 0.3 + \frac{0{,}62 Re_D^{\frac{1}{2}} Pr_D^{\frac{1}{3}}}{[1+(0{,}4/Pr_D)^{\frac{2}{3}}]^{\frac{1}{4}}} \left[1 + \left(\frac{Re_D}{282{,}000}\right)^{\frac{5}{8}}\right]^{\frac{4}{5}} \quad (18)$$

where:

- Nu_D is the Nusselt number with characteristic length the external diameter of the heat pipe at the condenser/evaporator section;
- Re_D is the Reynolds number with characteristic length the external diameter of the heat pipe at the condenser/evaporator sections;
- Pr_D is the Prandtl number with characteristic length the external diameter of the heat pipe at the condenser/evaporator section.

As first analysis air was initially used as a secondary fluid, but later on helium is also used. As already mentioned at the beginning of the study, an inlet temperature of 880 K was hypothesized for the FLiBe, which will decrease along its travel inside the heat exchanger. In this model, the heat exchange of a generic heat pipe which is located at the inlet section of the heat exchanger has been analyzed, therefore with the coolant still at 880 K and the air at 820 K, which is the preset outlet temperature.

The heat transfer coefficients of air and FLiBe were computed with equation (18) above within the Comsol model, where the properties of air and FLiBe are taken at a temperature equal to $T = \frac{T+T_{\text{air},\infty}}{2}$, where T is the temperature on the outer surface of the condenser. The density of the air has been obtained under the ideal gas assumption, obtaining a heat convective coefficient equal to 169.7 [W/m^{2}K]. The properties of FLiBe are reported in Table 5: thanks to its higher conductivity and viscosity with respect to air, the convective coefficient found is one order of magnitude higher than the one of air, and equal to 2340.9 [W/m^{2}K] [17].

Table 5. Thermodynamic properties of FLiBe [17].

	c_p [kJ/kgK]	μ [Pa·s]	k [W/m·K]	ρ [kg/m³]	v [m/s]	h [W/m²K]
FLiBe	2.386	$1.16 * 10^{-4} * exp(\frac{3755}{T})$	1.1	2413.03-0.4884*T	2.5	2340.9

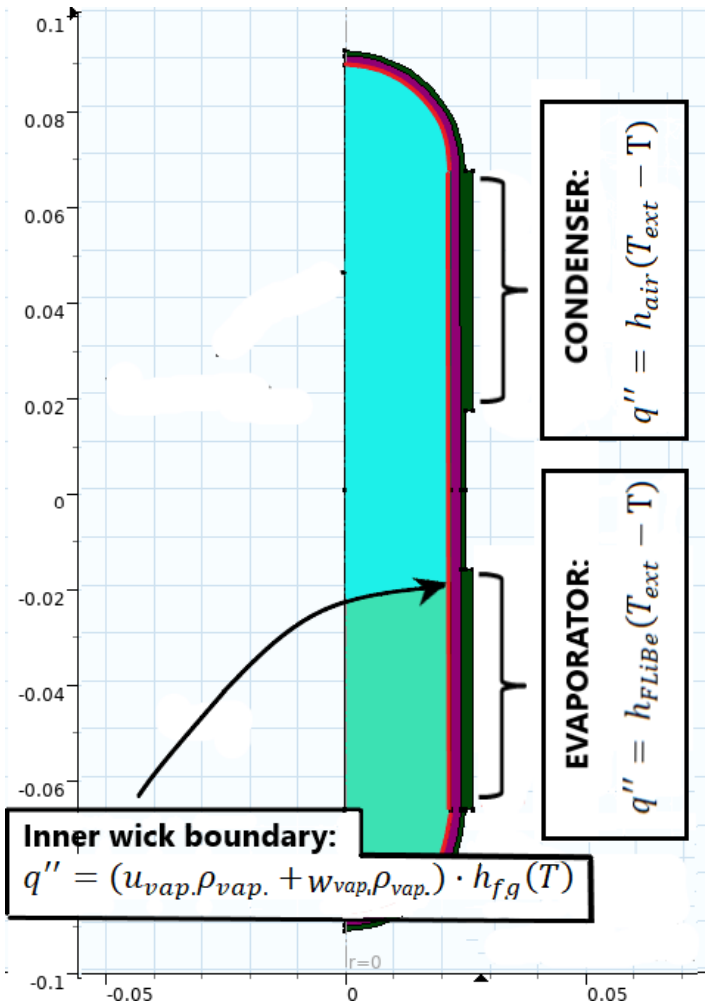

Figure 17. Boundary conditions for the solution of the thermal problem.

For the central axial line is imposed a symmetry condition, as it was for the fluid dynamic problem, and the remaining parts of the external surface of the heat pipe are thermally insulated, thus an adiabatic condition is imposed.

5.3. Sodium properties

Inside the heat pipe the sodium will be in saturation conditions or close to saturation, thus the temperature dependent correlations shown in Table 6 have been used for the sodium vapor and the liquid sodium.

Table 6. Sodium properties [18].

Properties	Property correlation	u.m
Enthalphy of vaporization	$h_{fg}(T) = 393.37 * \left(1 - \frac{T}{2503.7}\right) + 4398.6 * \left(1 - \frac{T}{2503.7}\right)^{0,29302}$	[kJ/kg]
Enthalpy of liquid sodium along the saturation curve	$H_{\sigma,liq.} - 365.77 + 1.6582 * T - 4.2395 * 10^{-4} T^2 + 1.4847 * 10^{(-7)} T^3 + 2992.6 * T^{-1}$	[kJ/kg]
Enthalpy of vapor sodium along the saturation curve	$H_{\sigma,vap.} = -365.77 + 1.6582 * T - 4.2395 * 10^{-4} * T^2 + 1.4847 * 10^{-7} * T^3 + 2992.6 * T^{-1} + 393.37 * \left(1 - \frac{T}{2503.7}\right) + 4398.6 * \left(1 - \frac{T}{2503.7}\right)^{0.29302}$	[kJ/kg]
Vapor pressure	$p_{vap.}(T) = (exp(11.9463 - 12633.7/T - 0.4672 * log(T)))$	[MPa]
Liquid density	$\rho_l(T) = 219 + 275.32 * \left(1 - \frac{T}{2503.7}\right) + 511.58 * \left(1 - \frac{T}{2503.7}\right)^{0.5}$	[kg/m³]
Vapor pressure derivative over temperature	$\Upsilon_\sigma(T) = \left(\partial p_{vap.} / \partial T\right)_\sigma = \left(\frac{12633.7}{T^2} - \frac{0.4672}{T}\right) exp(11.9463 - \frac{12633.7}{T} - 0.4672 * log(T))$	[MPa/K]
Vapor density	$\rho_g = \left(\frac{h_{fg}(T)}{T\Upsilon_\sigma(T)} + \frac{1}{\rho_l}\right)^{-1}$	[kg/m³]
CTE of the liq. sodium along saturation curve	$\alpha_{\sigma,liq.} = -\left(\frac{1}{\rho_l}\right)\left(\frac{\partial \rho_l}{\partial T}\right)$	[1/K]
CTE of the vap. sodium along saturation curve	$\alpha_{\sigma,vap.} = -\left(\frac{1}{\rho_{vap.}}\right)\left(\frac{\partial \rho_{vap.}}{\partial T}\right)$	[1/K]
Heat capacity of liq. sodium along saturation curve	$C_{\sigma,liq.} = \left(\frac{\partial H_{liq.}}{\partial T}\right)_\sigma - \left(\frac{\Upsilon_\sigma}{\rho_{liq.}}\right)$	[kJ/kg]
Heat capacity of vap. sodium along saturation curve	$C_{\sigma,vap.} = \left(\frac{\partial H_{vap.}}{\partial T}\right)_\sigma - \left(\frac{\Upsilon_\sigma}{\rho_{vap.}}\right)$	[kJ/kg]

Adiabatic compressibility	$\beta_s = 1{,}717 * 10^{-4}\ \frac{1+\frac{\theta}{3.2682}}{(1-\theta)}$; where $\theta = \left(\frac{T-371}{2503.7-371}\right)$	[1/MPa]
Isothermal compressibility	$\beta_T = \frac{\beta s C_{\sigma,liq.} + \left(\frac{T}{\rho liq.}\right)\alpha_\sigma(\alpha_\sigma + \beta_s \Upsilon_\sigma)}{C_{\sigma,liq.} - \left(\frac{T}{\rho liq.}\right)\Upsilon_\sigma(\alpha_\sigma + \beta_s \Upsilon_\sigma)}$	[1/MPa]
CTE of the liq. sodium	$\alpha_{P,liq.} = \alpha_\sigma + \beta_T \Upsilon_\sigma$	[1/K]
Heat capacity at constant pressure of liquid sodium	$C_{P,liq.} = C_{\sigma,liq.} + \left(\frac{T \alpha_{P,liq} \Upsilon_\sigma}{\rho_{liq.}}\right)$	[kJ/kg]
Heat capacity at constant volume of liquid sodium	$C_{V,liq.} = C_{P,liq.}\left(\frac{\beta_S}{\beta_T}\right)$	[kJ/kg]
Heat capacity at constant pressure of vapor sodium	$C_{P,vap.} = C_{\sigma,vap.} + \left(\frac{T \alpha_{P,vap.} \Upsilon_\sigma}{\rho_{vap.}}\right)$	[kJ/kg]
Thermal pressure coefficient	$\Upsilon_V = \left(\frac{12905.6}{T^2} - \frac{0.45824}{T} + 2.0949 * 10^{-3} + 2 * (-5.0786 * 10^{-7}) * T\right) * exp\left(8.35307 - \frac{12905.6}{T} - 0.45824 * log(T) + 2.0949 * 10^{-3} * T - 5.0786 * 10^{-7} * T^2\right)$	[MPa/K]
CTE of the vapor sodium	$\alpha_{P,vap.} = \left\lvert \frac{\alpha_{\sigma,vap.}}{1 - \frac{\Upsilon_\sigma}{\Upsilon_V}} \right\rvert$	[1/K]
Heat capacity at constant volume of vapor sodium	$C_{V,vap.} = C_{P,vap.} - \left(\frac{T \alpha_{P,vap.} \Upsilon_V}{\rho_{vap.}}\right)$	[kJ/kg]
Dynamic viscosity of liquid sodium	$\mu_{liq.} = exp(-6.4406 - 0.3958 * log(T) + \frac{556.835}{T})$	[Pa*s]
Dynamic viscosity of vapor sodium	$\mu_{vap.} = 1*10^{-5}$	[Pa*s]
Thermal conductivity of liquid sodium	$k_{liq.} = 124.67 - 0.11381 * T + 5.5226 * 10^{-5} * T^2 - 1.1842 * 10^{-8} * T^3$	[W/(m*K)]
Thermal conductivity of vapor sodium	$k_{vap.} = 0.041$	[W/(m*K)]

5.4. Results and discussion

The results obtained with the stationary model described in the previous paragraph are analyzed below. As a preliminary consideration, it can be noted that the power exchanged to the evaporator and the condenser is expected to be the same since the rest of the external surface of the pipe is thermally insulated. As can be seen from Table 5, however, the convective coefficient on the side of the FLiBe is two orders of magnitude higher compared to the one of air. It is therefore expected, looking at the Neumann's BC applied on the evaporator/condenser sections, that the temperature along the external wall in the condenser/evaporator regions will be very close to the one of FLiBe, in order to exchange the same amount of heat (Figure 18).

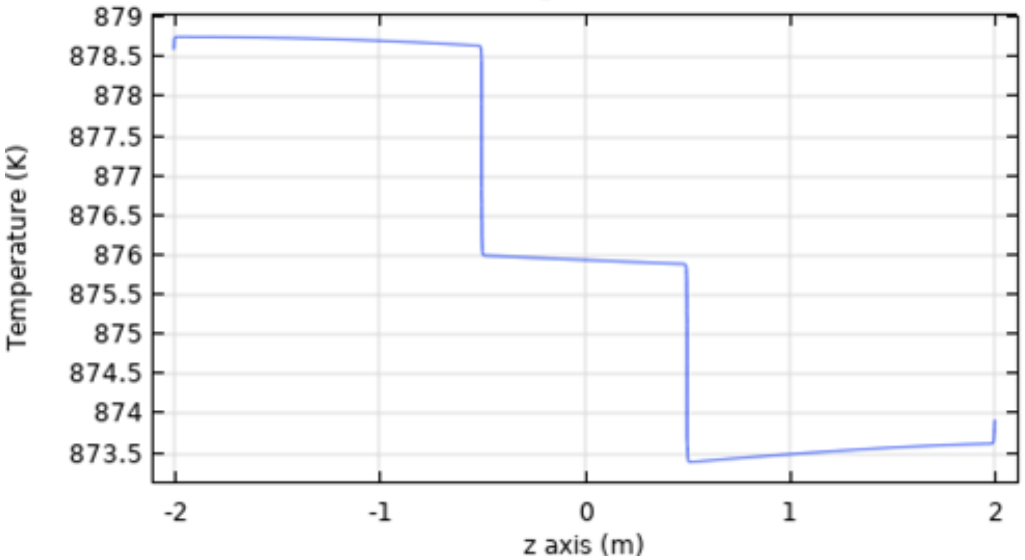

Figure 18. Temperature along the external wall of the heat pipe.

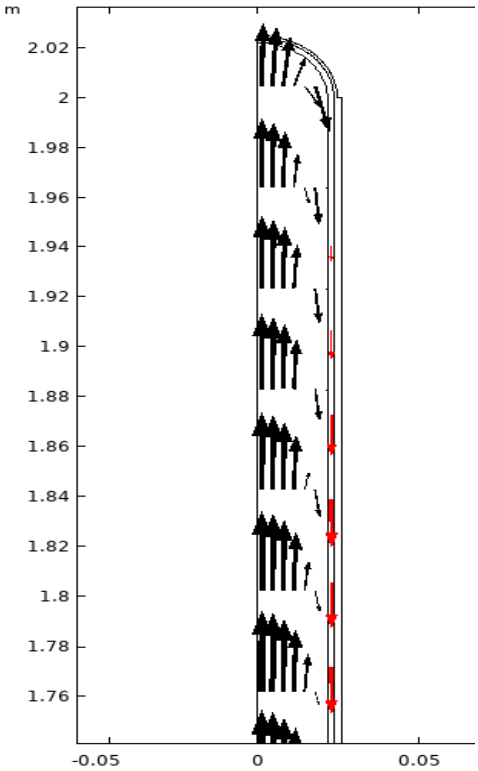

Figure 19. Arrow plot of the path of the flow inside the vapor cavity and the wick.

In Figure 19 it is possible to notice the arrow plot for the velocity inside the vapor cavity, as it is possible to notice the vapor change its direction at the evaporator section, passing from a laminar flow exclusively in a vertical direction, to a radial flow near the wick inner surface (the same consideration can be done at the condenser). The arrows in figure are proportional to the magnitude of the velocity in that point. From the simulation results the velocity of the vapor in the middle of the tube, where it reaches its maximum, is around 60 m/s, and the entire heat pipe is able to exchange 2.269 kW of thermal power at the evaporator/condenser section.

The value of the heat power obtained seems to be quite low. The limiting term of the heat pipe performance is the convective coefficient on the air side, which is very low. In order to improve it, some fins on the external surface can be added to enhance the heat transfer. Before trying to improve the design of the heat pipe, as it will be done later in this study, another approach for the determination of the convective coefficient was used, since the Churchill-Bernstein's correlation sometimes leads to non-negligible errors, due to the fact that the formula remains valid for a very large range of the Reynolds number. To calculate the heat

convective coefficient another Comsol model has been implemented, considering a 2D horizontal cross section of the condenser and by making it crossed by a turbulent flow of air, modeled as compressible. For the computation of the turbulent flow regime the K-ε model was used, which adds two components to the Navier-Stokes equations: the turbulent kinetic energy K and the turbulent dissipation rate ε. For the analysis of the heat exchange instead, the equation (16) for the heat transmission in fluids was used. The inlet velocity is the one of air (i.e. 10 m/s) and the temperature on the external wall of the pipe is taken equal to the average along the condenser external wall obtained with the previous model, equal to 873.53 K, with a no slip condition applied along the condenser wall. The obtained velocity field of air is shown in Figure 20.

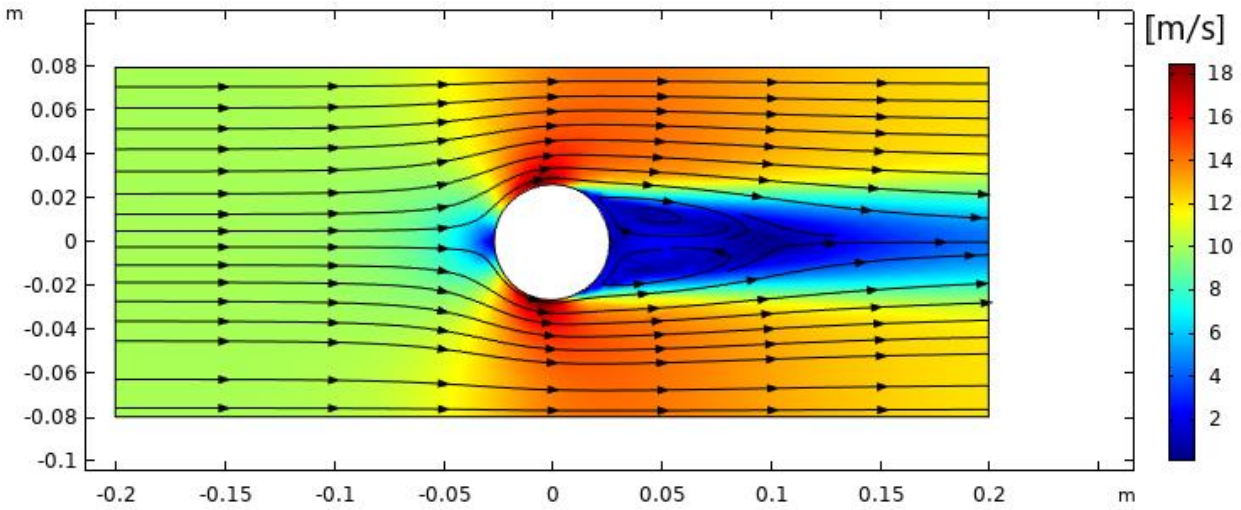

Figure 20. Streamlines of the air flow over the 2D horizontal cross section of the condenser.

The value of heat transfer rate exchanged between the pipe and the air is divided by the surface of the condenser and the temperature difference in order to obtain the value of the convective coefficient:

$$h = \frac{P_{hp}}{(\bar{T}_{wall,cond.} - T_{air,\infty}) * 2\pi L_{cond} R} = \frac{4{,}449.5}{(873.53 - 820) * 2\pi * 1.5 * 0.0265} = 346.26 \ [\mathrm{W/(m*K)}]$$

The value obtained with the Churchill-Bernstein equation then has been replaced by this new one in the 2D axisymmetric model of the heat pipe, practicing an iterative method by finding a new value of the average temperature at the condenser

and calculating again the heat transfer coefficient until convergence is achieved, with a prescribed tolerance of 0.1 K between two subsequent values of the average condenser temperature. The steps of the iterative process are reported in Table 7: at the end of the process a value of 347.16 W/(m^2∗K) for the convective coefficient was found, which allows to get 4.165 kW of power exchanged within a single heat pipe.

Table 7. Air heat transfer coefficient obtained with the 2D horizontal cross section model of the condenser.

ITERATIONS	h [W/(m²*K)]	$\overline{T}_{wall,cond.}$ [K]
1	169.7	873.53
2	346.26	868.07
3	347.16	868.05
Power exchanged (with h=347.16 [W/(m²*K)])		
4.165 kW		

The convective coefficient value found with method described above was then used, obtaining the following profiles of velocity, pressure and temperature inside the heat pipe.

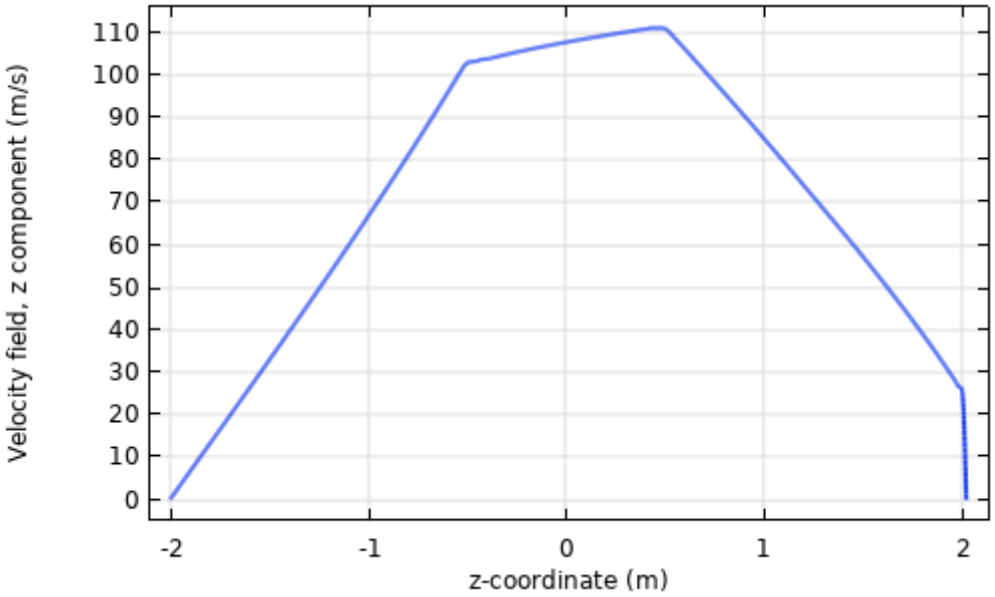

Figure 21. Velocity profile of the sodium vapor along the symmetry line of the heat pipe.

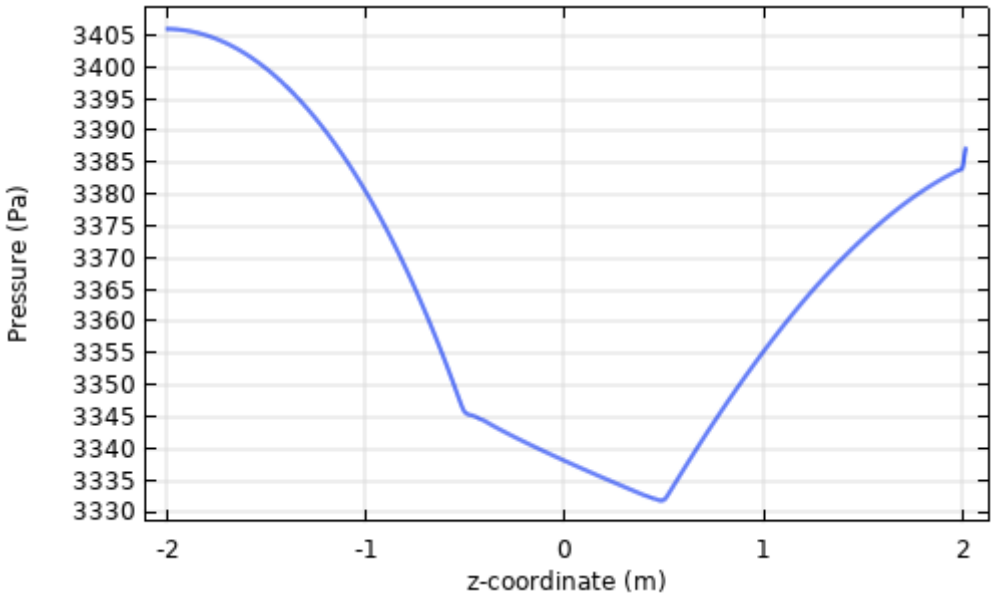

Figure 22.Pressure of the sodium vapor along the symmetry line.

As it possible to notice from Figure 21, the axial speed of the vapor along the symmetry line reaches its maximum value (equal to about 110 m/s), in correspondence of the beginning of the condenser (i.e. z = 0.5 m). In this point also the minimum pressure of the vapor is reached, since the pressure difference is the driving force which puts in motion the vapor from the hottest region (i.e. higher pressure) to the coldest one. The maximum value of the axial speed is far from the sound speed of sodium at those temperatures (about 2265 m/s at 870 K), thus there will be no flow choking problems or other unwanted sonic phenomena. Sonic effects in the flow may still happen at the start-up of the heat pipe, where

the exchanged powers are much higher, as explained for the sonic limit in paragraph 3.3. However, the pressure is almost constant inside the vapor, being almost in isothermal conditions, as it can be noticed in Figure 25 from the temperature profile of the vapor along the axial line.

Since the model is stationary, the latent heat flux exchanged at the condenser/evaporator results to be symmetrical, by integrating the curve in Figure 23 along the z-axis. The curve represents the latent heat flux per unit of the inner wick surface and, by integrating it, the latent heat flux per unit of the circumferential length is obtained, for which the latent thermal power is symmetrical by definition, being the model considered 2D axisymmetric.

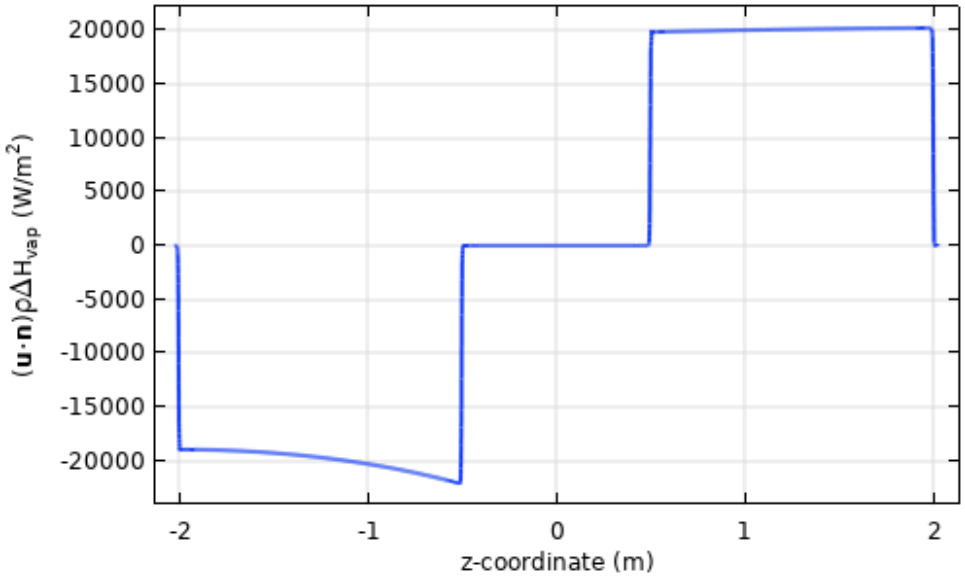

Figure 23. Latent heat flux from condensation/evaporation of the sodium, at the inner wick boundary.

The radial component of the velocity along the inner wick surface of the heat pipe represents the quantity of vapor/liquid which is subjected to phase change. As it possible to notice from Figure 24, the radial speed has the same profile of the heat latent flux, as the boundary condition on the inner wick boundary was defined as $q'' = (u_{vap.}\rho_{vap.} + w_{vap.}\rho_{vap.}) \cdot h_{fg}(T)$ [W/m^2], where $u_{vap.}$ is the radial component of the vapor velocity and $w_{vap.}$ is the axial one. The axial component is almost equal to zero at the condenser/evaporator sections, and in general along the vapor/liquid interface it assumes values one order of magnitude lower with respect to the radial speed.

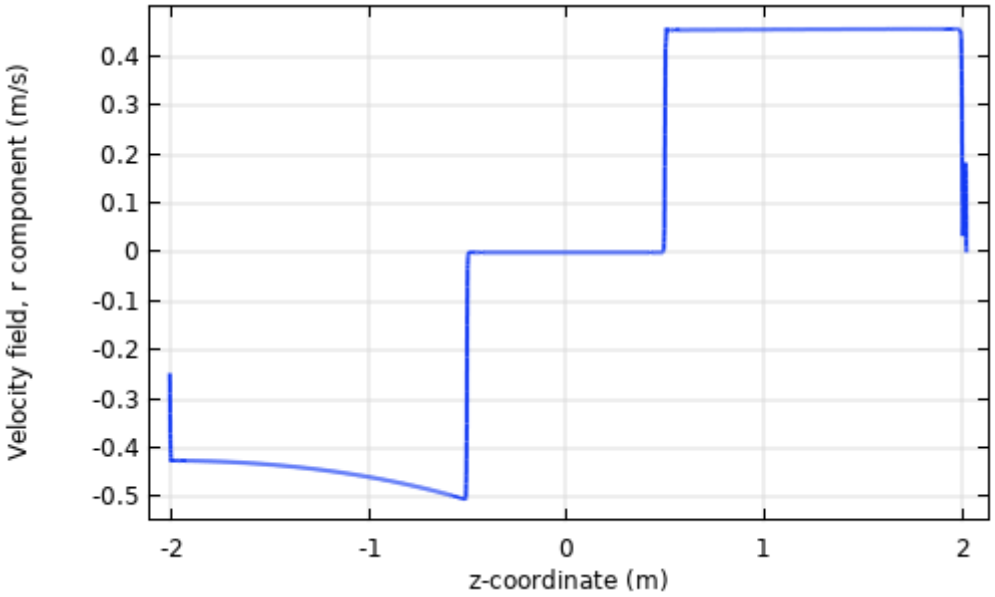

Figure 24. Radial component of the velocity at the inner wick boundary.

Finally, the temperature at different positions along the axis length is shown in Figure 25. As mentioned above the temperature in the vapor domain and at the liquid-vapor interface is almost constant as the vapor is in the saturation conditions. Along the external wall the temperature has an almost symmetric profile between the evaporator and the condenser with an intermediate value in the adiabatic region equal to about 872 K.

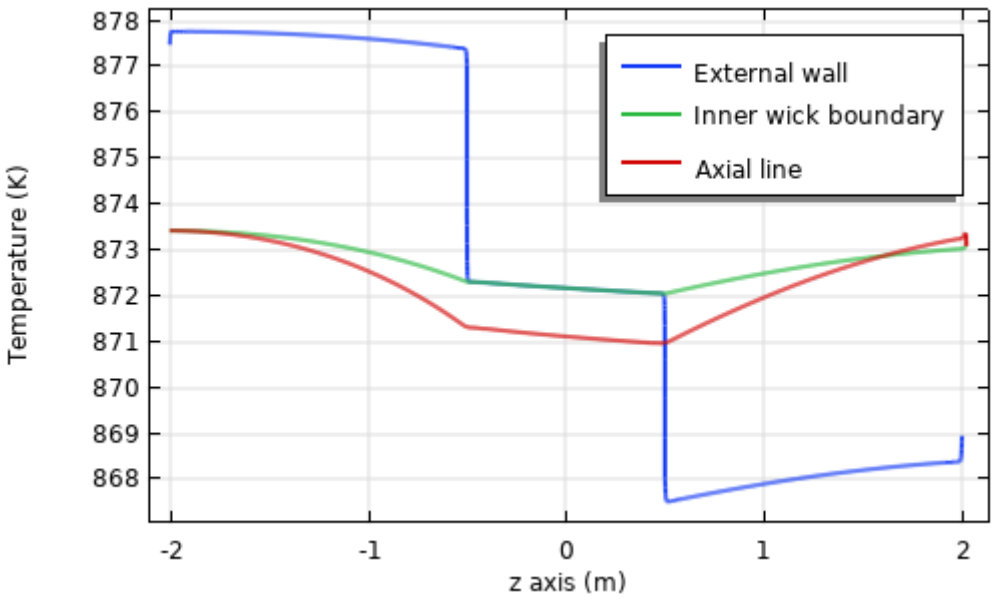

Figure 25. Temperatures at different locations of the heat pipe along z-axis.

5.4.1. Number of heat pipes inside the heat exchanger

To calculate the number of pipes needed inside the heat exchanger to transfer the thermal power necessary to bring the FLiBe back to 800 K, it would be necessary to consider a model of the entire heat exchanger, with the air and the coolant proceeding through the arrays of heat pipes in countercurrent. Therefore, it should be taken into account that inside the heat exchanger the temperature of the coolant will decrease as it proceeds through the heat pipes, while on the contrary the temperature of the air will increase with respect to the inlet section. The same is for the speed and pressure of the fluids, which will change from zone to zone along the heat exchanger. The value of the power exchanged in a single heat pipe found in the previous paragraph will not be exactly the same for all heat pipes on the bench. For sake of simplicity to calculate the number of heat pipes needed, it was assumed that the power found in the previous paragraph (i.e. 4.165 kW) is the same for all heat pipes:

$$N_{hp} = \frac{P_{th}}{P_{hp}} = \frac{630 * 10^6 W}{4165\ W} = 151{,}261$$

where:

- P_{th} is the thermal power provided inside the reactor to bring the FLiBe from 800 K to 880 K [W];
- P_{hp} is the power exchanged with a single heat pipe [W].

From a simple power ratio is obtained that about 150,000 heat pipes would be needed to bring the coolant back to the inlet temperature in the reactor. For a more reliable calculation of the number of heat pipes needed, it was considered another model which analyzes the heat exchange of a 2D horizontal section of the entire heat exchanger in the region of the evaporators. The equations used within the model are the same used for the calculation of the convective coefficient (Figure 20) of air, with the difference that now a series of heat pipes in rows is considered instead of a single heat pipe. The pipes are arranged in a triangular pattern, with a distance between the centers of the pipes equal to $\sqrt{2}D$, where D is the diameter

of the heat pipe at the evaporator/condenser sections. The flow regime analyzed is turbulent, with FLiBe entering at 2.5 m/s and 880 K, and with a removed heat flux on the outer surface of each pipe equal to the one found above divided by the external surface of the heat pipe, as shown in Figure 26.

$$q'' = \frac{-4{,}165\ W}{2\pi * 1{,}5\ m * 0.0265\ m} \quad [\mathrm{W/m^2}]$$

In order to reduce the computational cost only an array of 100 heat pipes is considered.

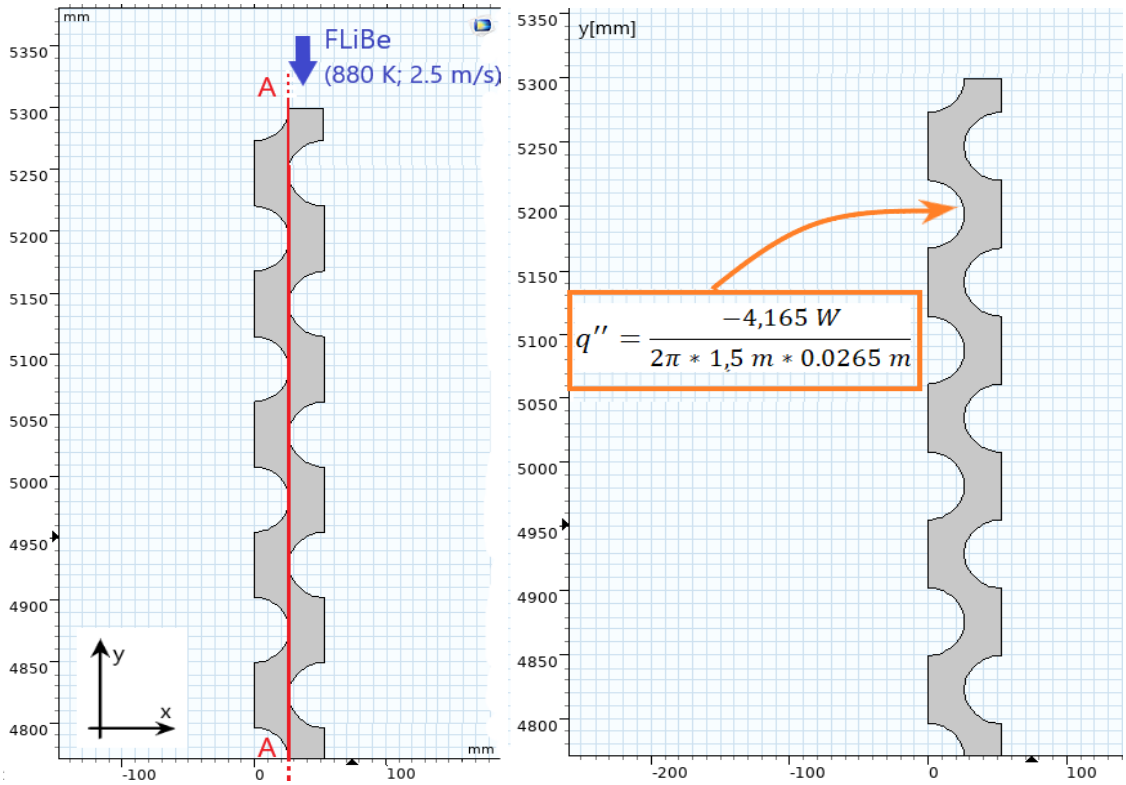

Figure 26 Computational domain of the inlet section of the 50 heat pipes array and boundary conditions applied.

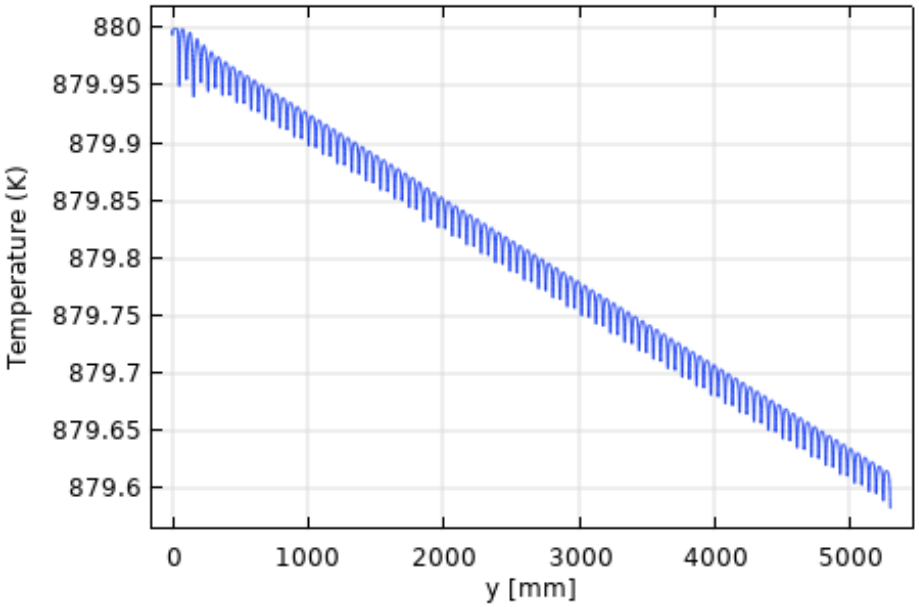

Figure 27. Temperature along section A.A. shown in figure 26 for the whole 50 heat pipes array.

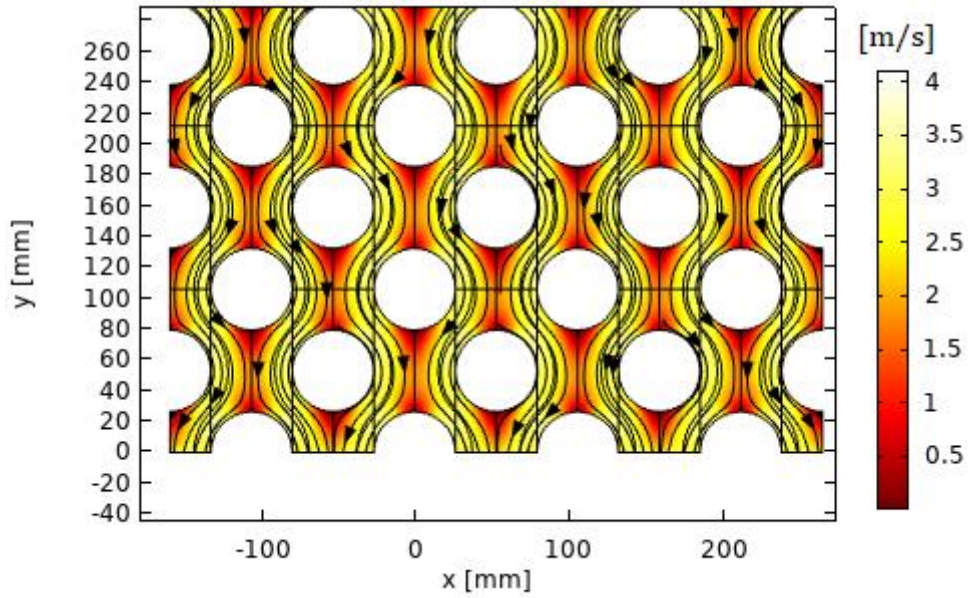

Figure 28. Velocity map and streamlines of the FLiBe at the outlet of the heat exchanger.

As it possible to notice from Figure 27, the temperature of the FLiBe along the heat exchanger decrease with periodic oscillations due to the lower temperatures obtained in the points closer to the pipes. The temperature profile, if taken along a trajectory that passes equidistant from the tubes along the heat exchanger, would appear linear, with an average temperature on the outlet section equal to 879.61 K. Making a ratio between the desired temperature drop (80 K) and the one

obtained with 100 heat pipes, it is possible to obtain the number of arrays needed to bring the coolant at the desired temperature of 800 K:

$$N_{arrays} = \frac{880\ K - 800\ K}{880\ K - 879.61\ K} = 205.13 \approx 206$$

Therefore approximately 206 sections like the one analyzed in the model will be needed. In total it means that the number of heat pipes in row must be equal to 20,600. Assuming now that there is only one coolant inlet section in the ARC reactor, this should be equal to the mass flowrate divided by the product of the density and velocity, assuming that in ARC the inlet conditions are the same of the heat exchanger:

$$A_{FLiBe,react.} = \frac{\frac{P}{cp * \Delta T}}{\rho_{FliBe} * V_{FliBe}} = \frac{\frac{630 * 10^6\ W}{2386 \frac{J}{kgK} * (880\ K - 800\ K)}}{2000 \frac{kg}{m^3} * 2.5 \frac{m}{s}} = 0.6601\ \mathrm{m}^2$$

The inlet section of the FLiBe in the model is a rectangular area with base equal to the diameter of the pipe and height equal to the length of the evaporator zone, thus equal to 0.053 m∗1.5 m = 0.0795 m^2. Dividing the total area of the reactor by the area of a single inlet sections of the heat exchanger, it is possible to find that 9 inlet sections will be needed to cool down the total coolant mass flowrate. sections of the salts in the exchanger. Therefore, the total number of pipes will be equal to:

$$N_{hp} = 9 * 20{,}600 = 185{,}400$$

The value obtained is slightly higher than the one obtained by simply dividing the power exchanged within the reactor by the one exchanged with a single heat pipe.

5.5. Design improvement of the heat pipe

In this chapter an analysis for the design improvement of the heat pipe will be carried out, with the aim of increasing the power exchanged, thus reducing the number of heat pipes to be used within the heat exchanger. As first modify to the design several fins have been applied on the external surface of the condenser, to increase the convective coefficient, which turned out to be an order of magnitude less than that of the FLiBe. Two different geometries are considered for the fins: first several longitudinal fins will be considered and then the performance obtained with radial arranged fins will be assessed.

Finally, an analysis of the entropy generation inside the different domains of the heat pipe will be performed, in order to draw some conclusions which will be used as suggestion for possible further modifications.

5.5.1. Application of rectangular longitudinal fins at the condenser

As first possible design improvement, 16 rectangular fins arranged longitudinally along the external surface of the condenser were analyzed. The fins taken into consideration have a rectangular cross section with base of 1 mm and height 6.5 mm. The model used to calculate the convective coefficient with the new geometry is the same used in the chapter 5.4 for calculating the convective coefficient without fins. The horizontal cross section of the condenser with the rectangular fins longitudinally arranged around the condenser is shown in Figure 29. The rectangular air domain was considered long and wide enough to be able to catch the disturbances of the flow and the turbulences generated downstream of the pipe. For the meshing 8 additional boundary layers were adopted on the whole external surface of the condenser, with a stretching factor equal to 1.2 (i.e. between two subsequent boundary layers the dimensions increase by 20%), as it were done in paragraph 5.1 for the inner wick boundary. This allows to better capture the gradients of speed and temperature and the creation of turbulences close to the finned surface.

The boundary conditions applied are the same used in paragraph 5.4, with a Dirichlet's BC set on the external surface of the condenser: the temperature imposed

is equal to the value found in the absence of fins (i.e. 868.05 K), using as convective coefficient 347.16 W/(m^{2}K) (Table 7).

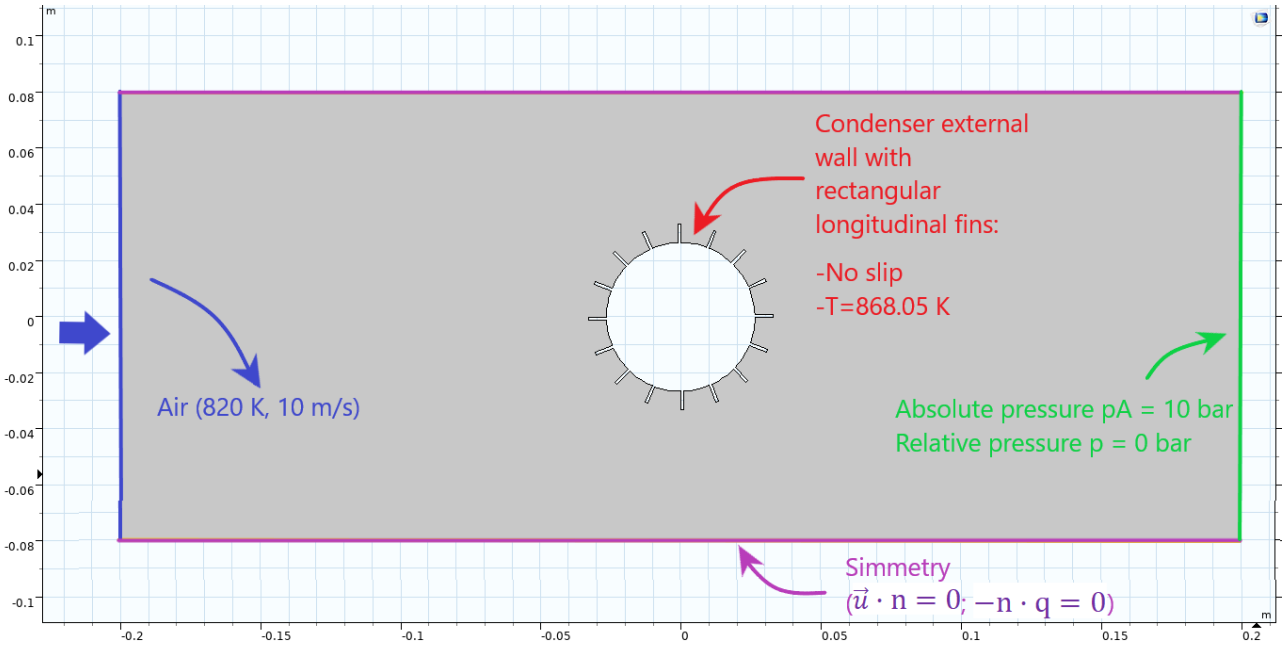

Figure 29. Computational domain and BCs for the calculation of the convective coefficient using rectangular longitudinally arranged fins.

Figure 30 shows the field of the air velocity along its passage in cross flow on the finned tube: it can be noticed that compared to the case without fins (Figure 20), the turbulent vortices created downstream of the pipe are much larger, with an extension equal to approximately the diameter of the pipe (along y-direction) and more extended along the flow direction. The presence of the fins in fact disturbs the field of motion of the air by creating two large symmetrical vortices. Furthermore, the fins create a flow shielding effect which, despite allowing for small eddies even between one fin and the other, greatly decreases the local speed of the flow and in some areas the speed of the air almost reaches values close to zero on the external surface of the condenser. In order to understand which are the critical regions of the finned surface that mostly hinder the heat exchange, different portions of the external wall of the condenser were analyzed, as shown in Figure 31: given the symmetry of the domain and boundary conditions, only the lower part of the pipe was considered.

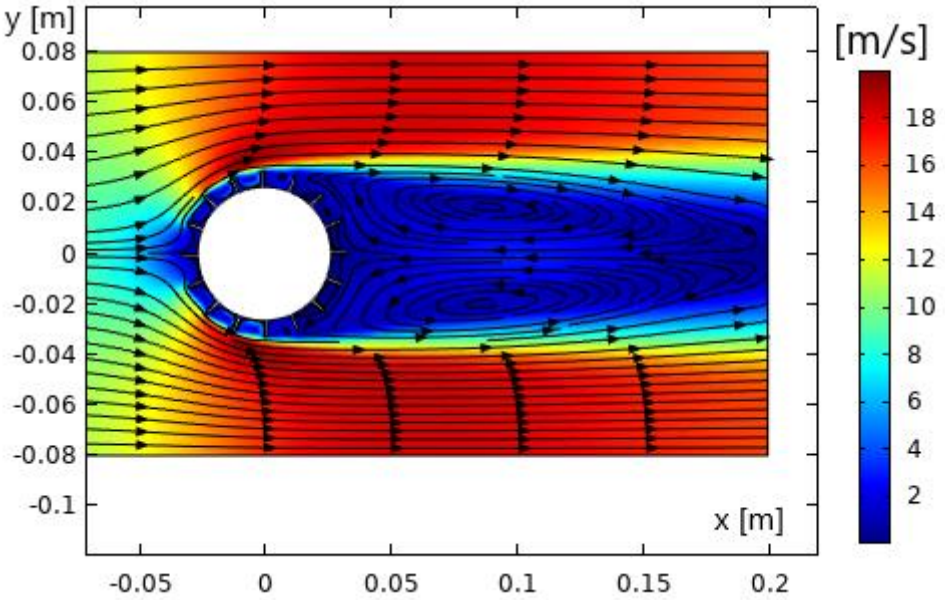

Figure 30. Velocity map and streamlines of air.

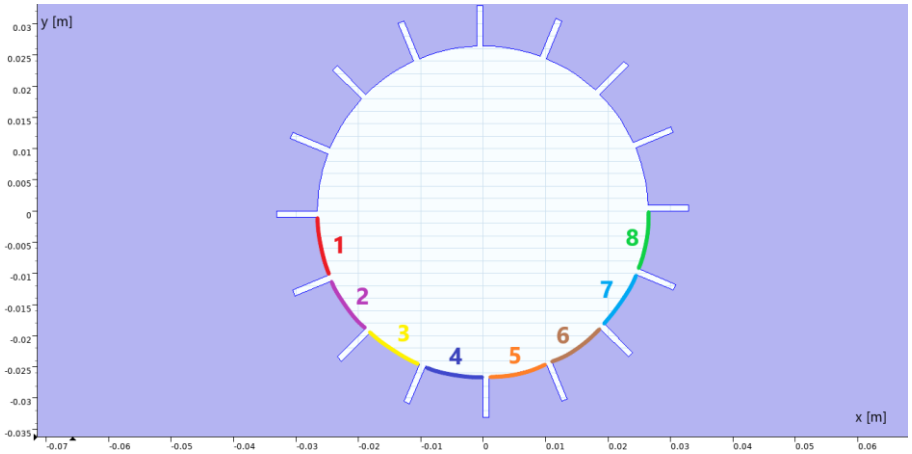

Figure 31. Portion of the external wall for which velocity is analyzed.

Figure 32 shows the magnitude of the velocity of the air along the arc lengths shown in Figure 31. Looking at the figure it can be seen that the portions of the condenser wall where the air reaches the highest speeds are sections 3 and 4, while not negligible values are achieved also in regions 2 and 5. The heat flux exchanged in the different portions (both convective and conductive), shown in Figure 34, leads to different results: the heat fluxes exchanged in regions 6,7,8 are not negligible even though the speed is almost null. What is concluded, looking at the magnitude of the temperature gradients in Figure 33, is that the phenomenon of heat exchange is governed by the conductive term in equation (16), being the

power exchanged in every portion absolutely valuably coherent with the magnitude of the temperature gradients.

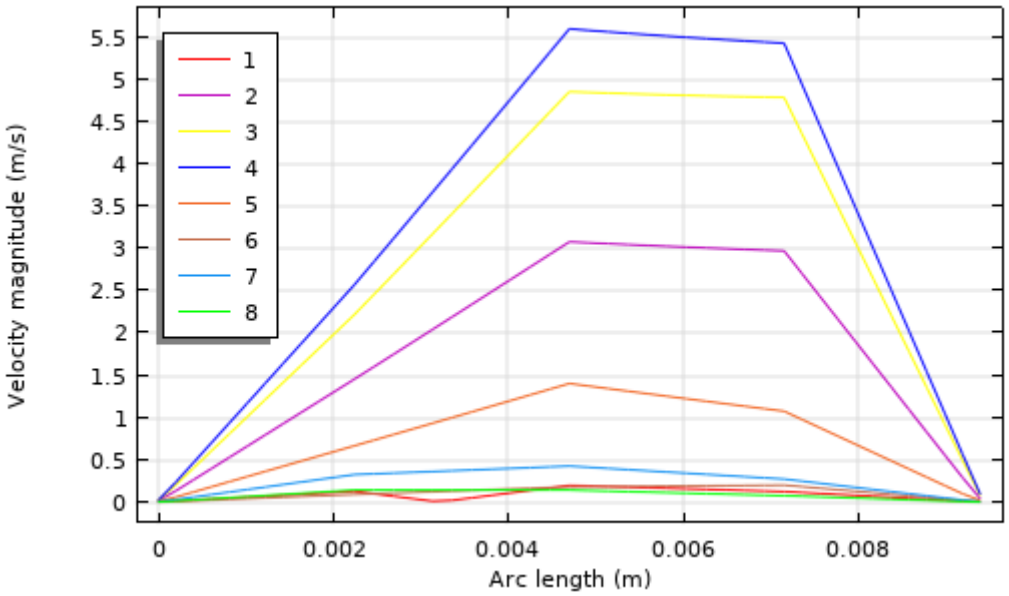

Figure 32. Velocity magnitude along the different portions of the condenser wall.

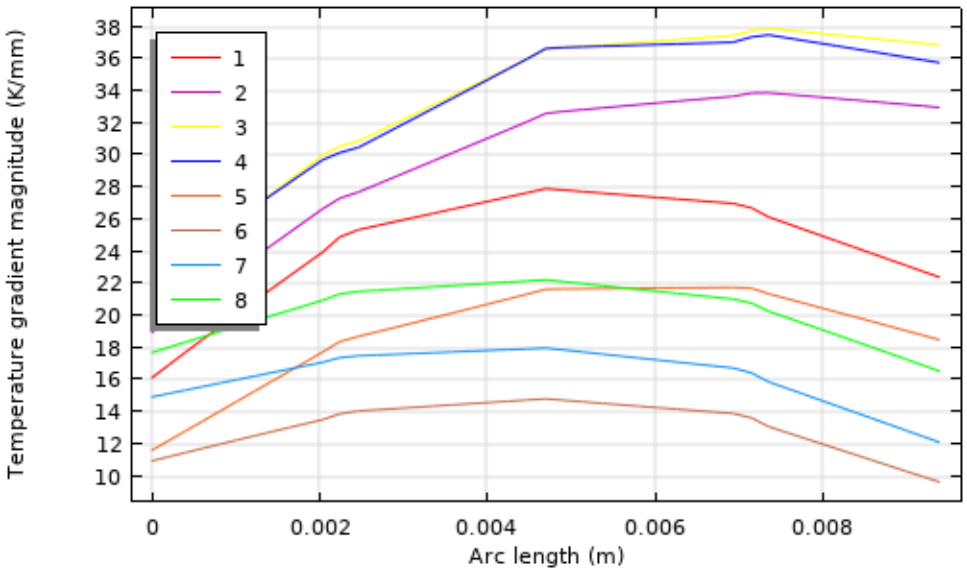

Figure 33. Temperature gradient magnitude along the different portions of the condenser wall.

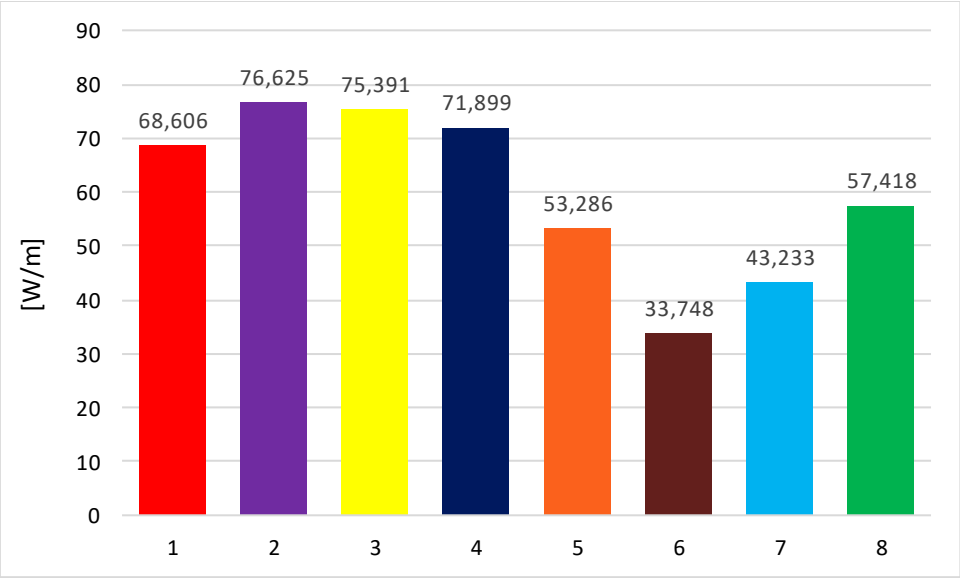

Figure 34.Heat fluxes exchanged per unit of axial length z.

The air velocities around the heat pipe are lower than the inlet velocity, assuming values in a range from 1 to 8 m/s. However, the total heat flux exchanged along the condenser external surface in the presence of the longitudinal fins is equal to 6.856 kW, which leads to a convective coefficient value equal to:

$$h_{long.} = \frac{P_{hp}}{\left(\overline{T}_{wall,cond.} - T_{air,\infty}\right) * A_{ext.}}$$

where:

- $\overline{T}_{wall,cond.}$ is the temperature imposed as boundary condition (i.e. 868.05 K), equal to the average temperature on the external wall of the condenser obtained with the model without fins;
- $T_{air,\infty}$ is the undisturbed temperature of the air, equal to 820 K;
- P_{hp} is the thermal power exchanged at the condenser with longitudinally arranged fins, equal to 6.856 kW;
- $A_{ext.}$ is the external surface including the fins, equal to 0.5618 m^2, which can be calculated as $A_{ext.} = N_{fins} * (A_{pipe} + A_{fins})$; where N_{fins} is the number of fins (i.e. 16). A_{fins} is the added surface due to the presence of the fins, calculated as $A_{fins} = L_{cond.} * \left(H_{fin} + 2 * L_{fin}\right)$, where H_{fin} is the height of the fins, L_{fin} is the length of the fins and $L_{cond.}$ is the length of the condenser (i.e. 1.5

m). $A_{pipe} = \left(2 * \pi * R_{cond.} - H_{fin} * N_{fins}\right) * L_{cond.}$ is the remaining exchanging external surface of the condenser after the addition of the fins.

The resulting value of the convective coefficient is equal to 253.98 W/(m^2∗K), which is quite lower than the one found without fins. However, this value must be corrected by applying an iterative method like the one used in Table 7. The iterative process consists in correcting the value of $\bar{T}_{wall,cond.}$ with a new one found using the convective coefficient just found above in the 2D axisymmetric model, and then using that value to find again a new convective coefficient with the model described above.

This iterative calculation was not carried out because the value of the convective coefficient found, using a $\bar{T}_{wall,cond.}$ value equal to the case without fins, is sufficiently low to affirm that this is not the optimal geometry for the application of interest. Therefore, in the following chapter another geometry for the fin is analyzed, applying a volume constraint in order to make a reasonable comparison using the same amount of material for the fins.

5.5.3. Application of radial fins at the condenser

The second geometry analyzed to improve the thermal exchange are fins arranged radially along the condenser. As mentioned above, to make a comparison with the longitudinal fins a volume constraint has been imposed:

$$V = V_{fin,rad.} = V_{fin,long.}$$

where $V_{fin,long.}$ is the volume of the fins in the previous case, equal to 1.56∗10^{-4} m^3, and calculated as $V_{fin,long.} = N_{fins} * H_{fin} * L_{fin} * L_{cond.}$. Imposing an axial thickness of the fins $t_{\mathrm{fin,rad.}}$ equal to 1 mm, a radial length R_{fin} of the fins equal to 8 mm and always considering an external radius of the condenser $R_{cond.}$ equal to 26.5 mm, the number of radial fins to be applied along the condenser was found:

$$N_{fins,rad.} = \frac{\mathrm{V}}{\pi * (\mathrm{R}_{fin}^2 - {R_{cond.}}^2) * t_{\mathrm{fin,rad.}}}$$

The rounded number of fins obtained is equal to 102: in order to be conservative in the comparison with the longitudinal fins, only 100 radial fins were considered, with an axial distance between two consecutive fins equal to 0.015 m.
The computational domain used for the radial fins is shown in Figure 35: unlike the longitudinal fins, it was necessary to implement a 3D model, in fact, due to the arrangement of the fins, a 2D horizontal cross section would not have represented the whole condenser. Due to symmetry, the domain is reduced to a single fin plus two condenser sections of length equal to half the distance that divides two consecutive fins.

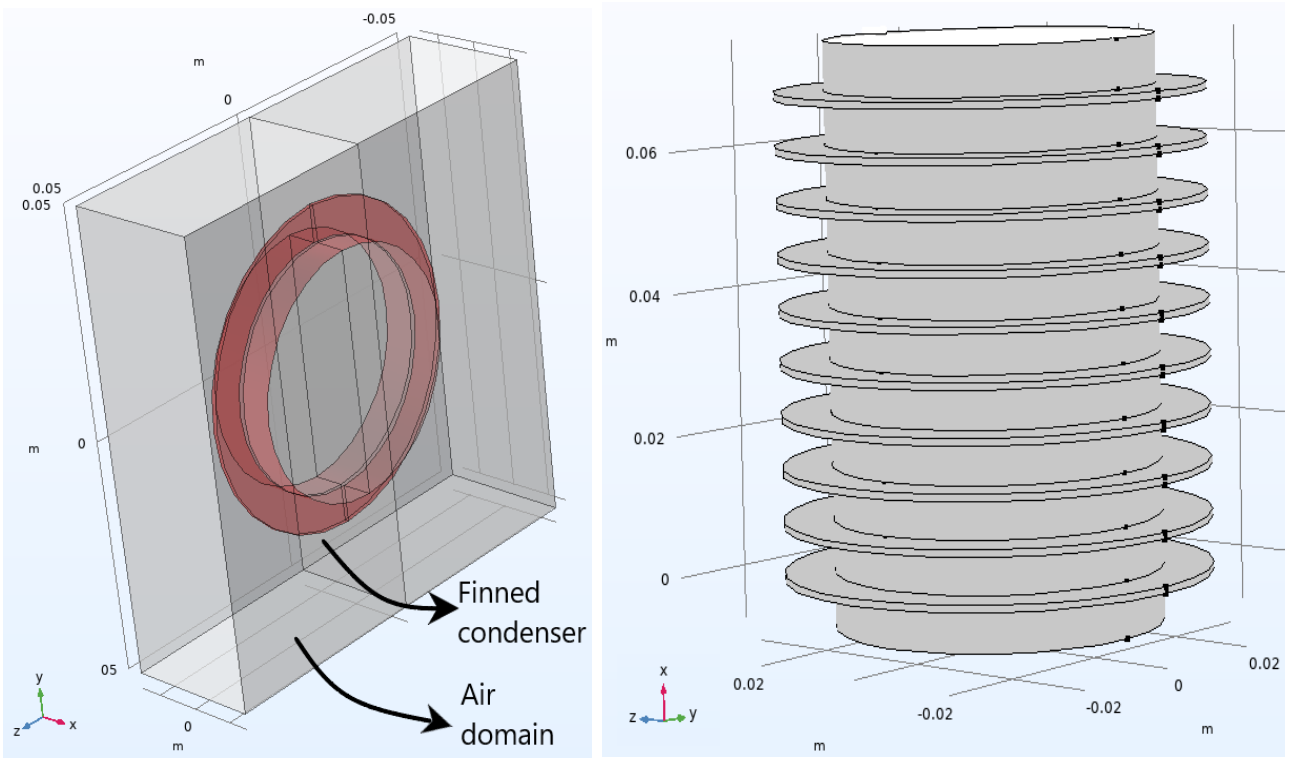

Figure 35. Computational domain (on the left) and 3D view of a section of the finned condenser (on the right).

The physics of the model and the boundary conditions are the same of the model used for the longitudinal fins, with the difference that now the boundaries are no longer segments but surfaces. By imposing, as in the previous case, a temperature on the external surface of the condenser equal to 868.05 K, it was obtained that the heat pipe would be able to exchange about 11.386 kW of thermal power. The convective coefficient was then found with the same equation used for the longitudinal fins (i.e. Newton's law), where $\overline{T}_{wall,cond.}$ and $T_{air,\infty}$ are the same of

previuos paragraph and P_{hp} is the heat flux exchanged. The external surface of the condenser in this case is equal 0.5614 m^2, and it has been calculated as:

$$A_{ext,rad.} = (\pi * (R_{fin}^2 - {R_{cond.}}^2) * 2 + 2 * \pi * R_{cond.} * H_{\text{fin,rad.}}) * N_{fins,rad.} + (2 * \pi * R_{cond.} * (L_{cond.} - N_{fins,rad.} * H_{\text{fin,rad.}}))$$

We therefore find an equal convective coefficient value equal to 422.09 W/(m^2∗K), with a good improvement with respect to the value found without fins (i.e. 347.16 W/(m^2∗K)). In order to obtain a more reliable values of the power exchange within a single heat pipe, the convective coefficient has been calculated with the same iterative approach described at Pag.43. The flow chart of the iterative process is shown in Figure 36:

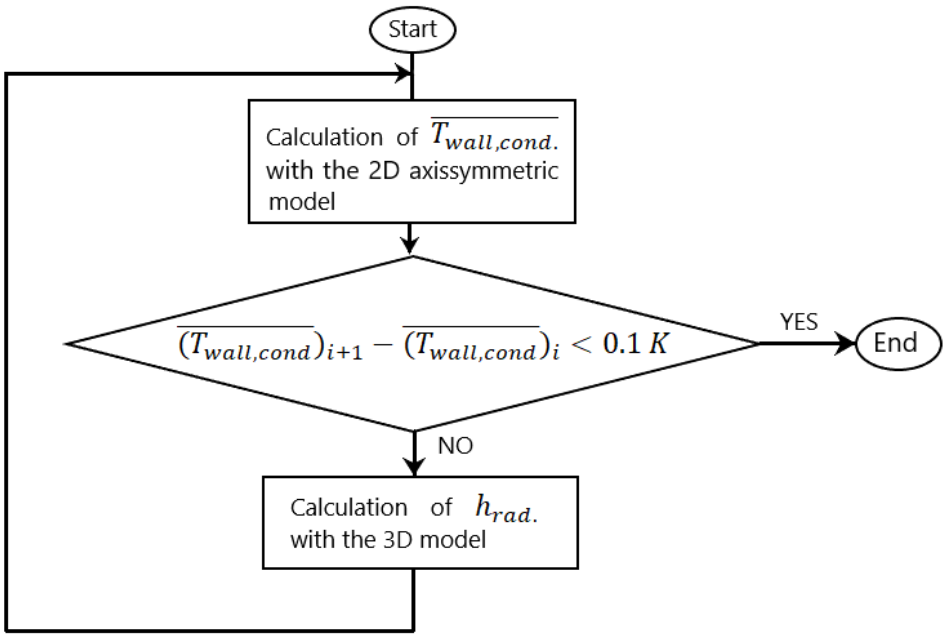

Figure 36. Flow chart of the iterative method used for the calculation of the convective coefficient.

The 2D axisymmetric model described in paragraph 5.4 was modified only by adding the radial fins along the condenser, while for the rest is remained exactly the same. At the end of the process, whose steps are summarized in Table 8, it has been obtained that the finned condenser is able to transfer 6.927 kW of thermal power, with a convective coefficient equal to 510.48 W/(m^2∗K). As expected, the addition of the radial fins led to a good improvement in the performance of the heat pipe. In Figure 37 is shown the streamline plot together with the magnitude of the air velocity over the finned surface of the condenser. As in the case of the longitudinal

fins, two vortices are created downstream of the condenser, but of smaller dimensions. The speeds downstream of the tube are no longer negligible as in the case of the longitudinal fins, while there are areas of the condenser surface where the speed reaches 18 m/s.

Table 8. Iterative steps for the calculation of the convective coefficient.

ITERATIONS	$\overline{T}_{wall,cond.}$ [K]	P_{hp} [W]	$h_{rad.}$ [W/(m²*K)]
1	868.05	11,386	422.09
2	846.26	7,318.6	496.44
3	844.47	6,983	508.32
4	844.21	6,934.2	510.19
5	844.17	6,926.7	510.48

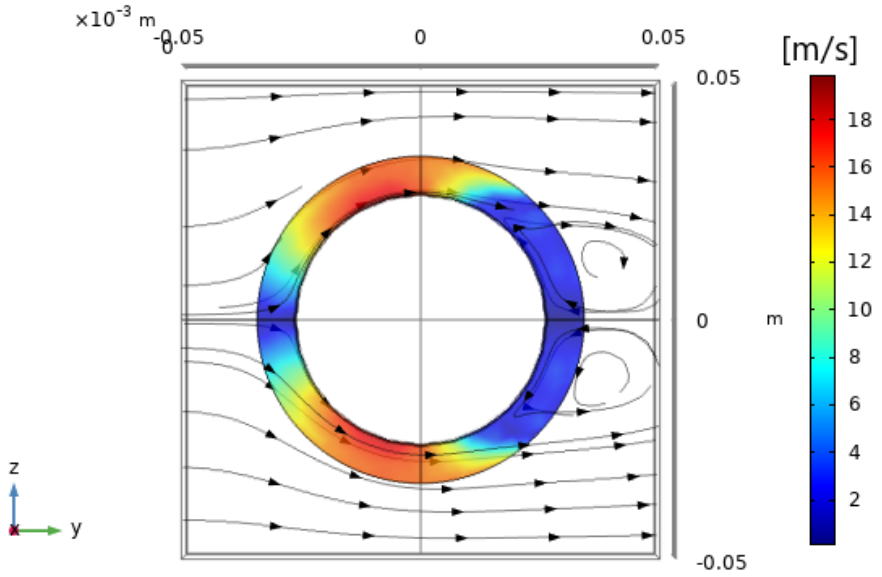

Figure 37. z-y view of the velocity field with temperature map over the finned condenser.

5.5.3.1. *Optimal inclination of the radial fins*

In this section a parametric analysis will be performed, by varying the angle of inclination of the radial fins, as a result of the rotation around the z axis of Figure 35. Different values of the convective coefficient were found for five different values of the angle of inclination assigned in the range 0°-15°. Then a five-equations linear system was solved to find the coefficients of a fourth degree polynomial that approximates the curve. Subsequently other different values were assigned to the inclination (control values) to see if the curve found effectively well approximates the different values obtained for the convective coefficient. As Figure 38 shows the convective coefficient reaches the higher value of about 520 W/(m^2∗K) for an inclination angle equal to 12.3°. However, even if a small improvement is achieved using inclined fins it may turn out that it is not a good compromise from the point of view of the manufacturing process of the heat pipes.

For the purpose of this study, that wants to optimize as much as possible the heat exchange, is considered from now on an angle of 12.3° but the consideration made above should not be neglected in the design phase of a similar heat exchanger.

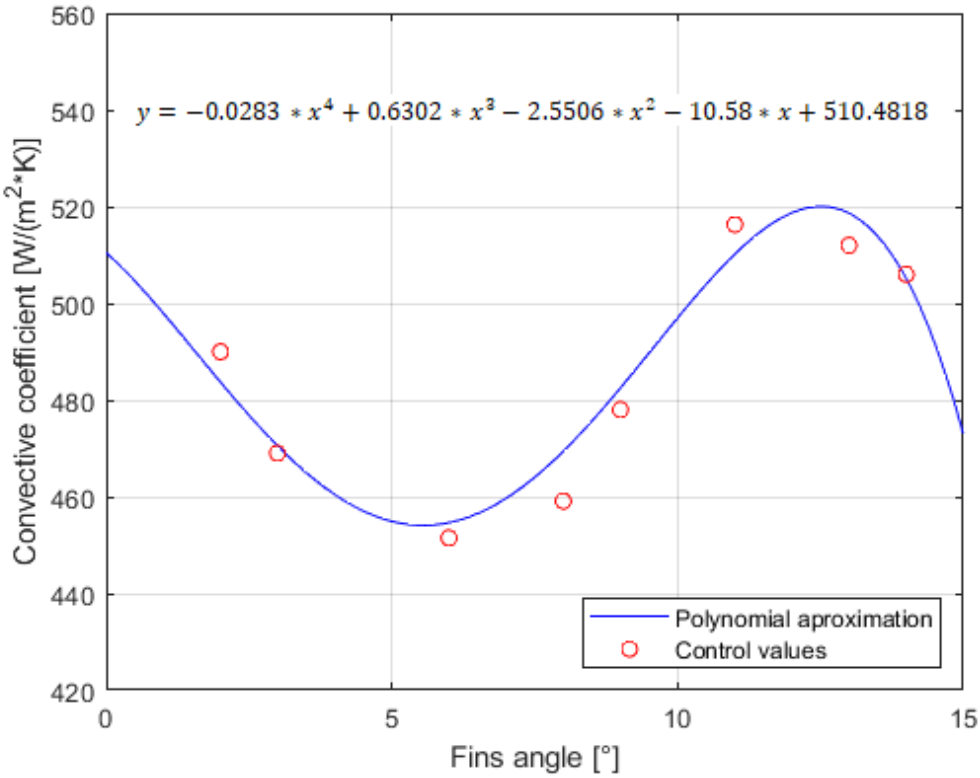

Figure 38. Convective coefficient as function of the inclination of the fins.

5.5.3.2. *Helium as secondary fluid*

In the previous chapter two different geometries have been analyzed for the implementation of fins on the external surface of the condenser, thus modifying the geometry of the heat pipe to try to increase the heat exchange in an area where the convective coefficient due to the forced convection of the air was relatively low. In particular, it was found that the radial fins offer better performance than the longitudinal ones, considerably increasing the convective coefficient. This chapter evaluates how the performance of the heat pipe varies, no longer by modifying the geometry, but by modifying the secondary fluid to be used in the power cycle. In particular, as described in paragraph 3.2.1, helium at 25 bar will be analyzed as a secondary fluid to be used within the same power cycle shown in Figure 13. Similarly to what was done for air, the helium flow was considered turbulent and compressible, with an inlet velocity in the exchanger equal to 10 m/s. If the same radial fins used for air are adopted, it is possible to obtain the values summarized in Table 9 through the same iterative process (Figure 36), using helium instead of air. Obviously this would result in a reduction in the size of the heat exchanger as a single heat pipe would be capable of carrying more thermal power. However, this design choice could lead to higher fixed costs in addition to operating ones, which will be higher as helium would certainly be more expensive than air. Inside the exchanger, in fact, it may be necessary to adopt more resistant joints and materials, as well as a greater thickness of the walls of the heat pipe and of the walls of the heat exchanger to prevent helium leaks, thus increasing the investment cost.

Table 9. Iterative steps for the calculation of the convective coefficient, using helium as secondary fluid and radial fins inclined by 12.3°.

ITERATIONS	$\overline{T}_{wall,cond.}$ [K]	P_{hp} [W]	h [W/(m²*K)]
1	868.05	17,523	649.03
2	841.89	8,361.5	688.64
3	841.26	8,139	690.2
4	841.24	8,130.3	690.3

5.5.4. Exergetic analysis

Entropy generation analysis is a powerful tool in the design phase, as it allows to identify possible suggestions to improve the system performance, suggesting which are the objective functions or the parameters to use as free variables in the optimization process. In particular, a 2D mapping of the entropy generation will be created within the 2D vertical cross section of the system, using the axisymmetric model described in chapters 5.1 and 5.2, with the only addition of the radial fins to the condenser and therefore using the value of the convective coefficient found in the previous paragraph with helium at 25 bar. The generation of entropy can be divided into several contributions, each of them referring to a different physical phenomenon, such as viscous dissipation, mass transport or heat transmission. The contributions due to mass transport and viscous dissipation within the wick and core vapor were negligible compared to the term related to heat transmission.
The entropy generation, due to heat transmission phenomena, is written in a local formulation as follow:

$$\sum_{irr}''' = -k \cdot \nabla \mathrm{T} \cdot \frac{-\nabla \mathrm{T}}{T^2} = \mathrm{k} \cdot \frac{(\nabla \mathrm{T})^2}{T^2} \quad [\mathrm{W/(m^3K)}]$$

The map of the entropy generation in the different heat pipe domains is shown in Figure 39. As it is possible to see the more critical regions from an entropy generation point of view are the portions of the wick and the external wall where the fins are placed, since these regions experience the highest temperature gradients. As seen from the above equation, the generation of entropy strongly depends on the temperature gradient, as it appears squared in the equation.

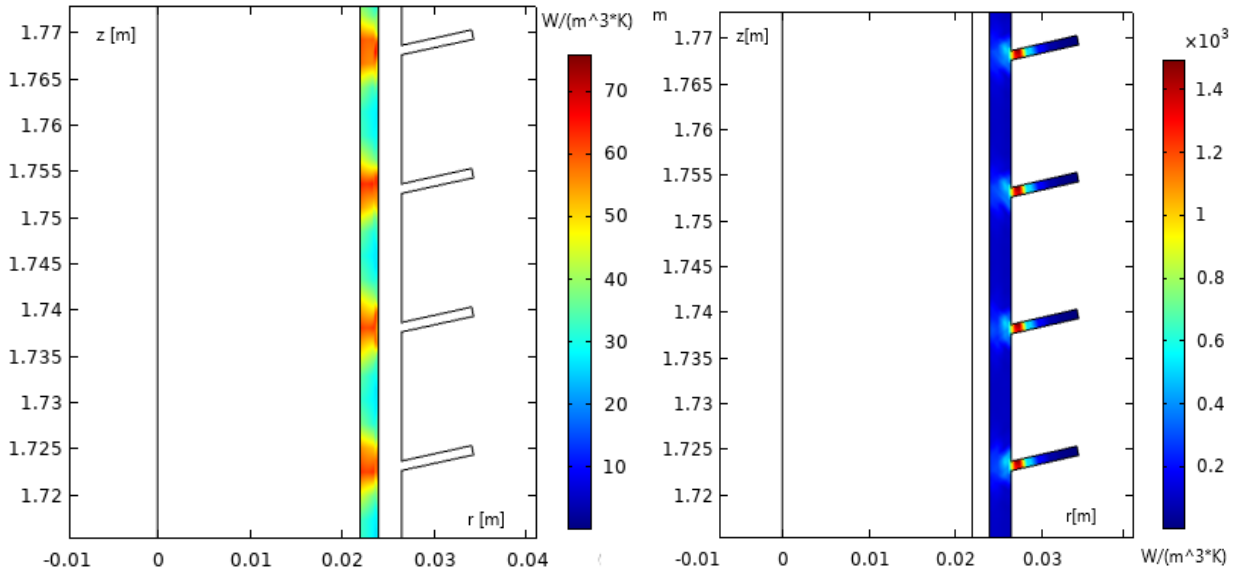

Figure 39. Entropy generation map inside the wick and the external wall along a section of the finned condenser.

5.5.4.1. Optimal wick thickness

In order to improve the design of the heat pipe it was chosen to change the thickness of the wick, looking at how it affects the generation of entropy. For the exergetic optimization, the goal is to obtain a more homogeneous map of the entropy generation, avoiding having areas with high temperature gradients, and therefore with a greater destruction of exergy. The total generation of entropy within the volume considered together with a second parameter is therefore considered for the optimization. A more homogeneous distribution does not necessarily imply an improvement in the design, as the reduction of destroyed exergy could be due only to a lower thermal power exchanged. The exchanged power is therefore used as the second parameter: the optimization process is based on searching for the value of the wick thickness which allows to obtain the lowest generation of entropy together with the highest thermal power exchanged. Since the external surface of the heat pipe will increase with the increase of the wick thickness, being fixed all the other geometrical parameters (vapor core radius, external wall thickness), the objective function for the optimization process will be the ratio between the total entropy generated within the wick and the thermal power exchange. In this way it is possible to take into account that also the surface exposed to the forced convenction is changing together with the wick thickness.

Therefore, three different values were assigned to the wick thickness (2 mm, 3 mm, 4 mm) and then the parabolic curve passing for these three points was found solving a simple linear system in order to find the coefficients of the second degree equation. As can be clearly noticed from the Figure 40, the optimal value of the thickness is 3.1 mm, as it allows to obtain the lowest entropy generation to thermal power ratio.

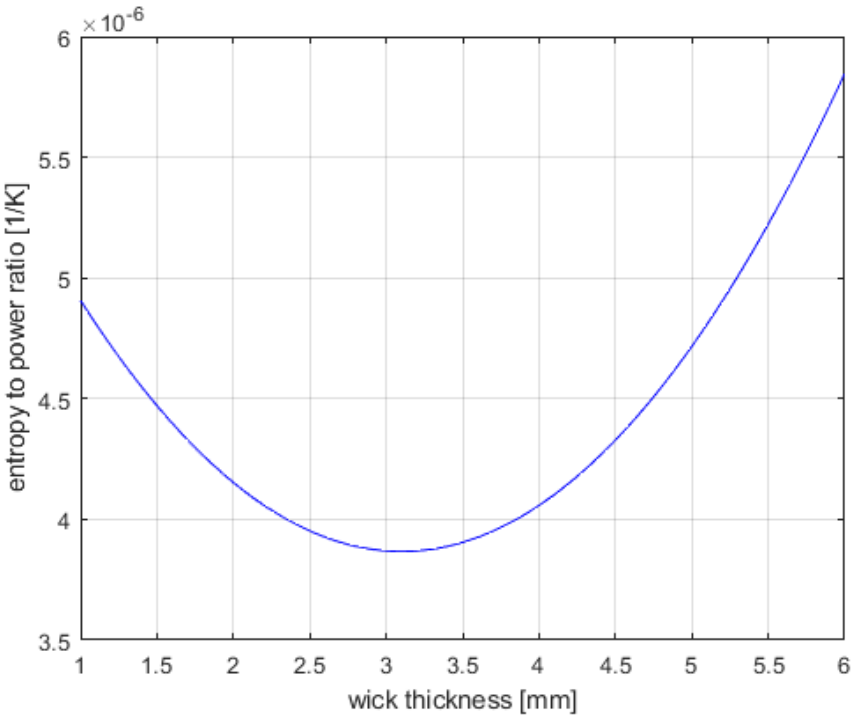

Figure 40. Ratio between the total entropy generated inside the wick and the power exchanged as function of the wick thickness.

The thermal power value obtained if a wick thickness equal to 3.1 mm is adopted is equal to 8.668 kW. Furthermore, increasing the thickness of the wick, leads also to an increase of the capillary limit described in the paragraph 3.3, as the term A_w increase within the equation (10). For a heat pipe of the size considered in the previous analysis, with a wick thickness of 3.1 mm, the operating limits shown in Figure 41 are obtained. How it can be seen in the figure, for the considered geometry, the capillary limit is the only limit to be kept in consideration for temperatures above 800 K.

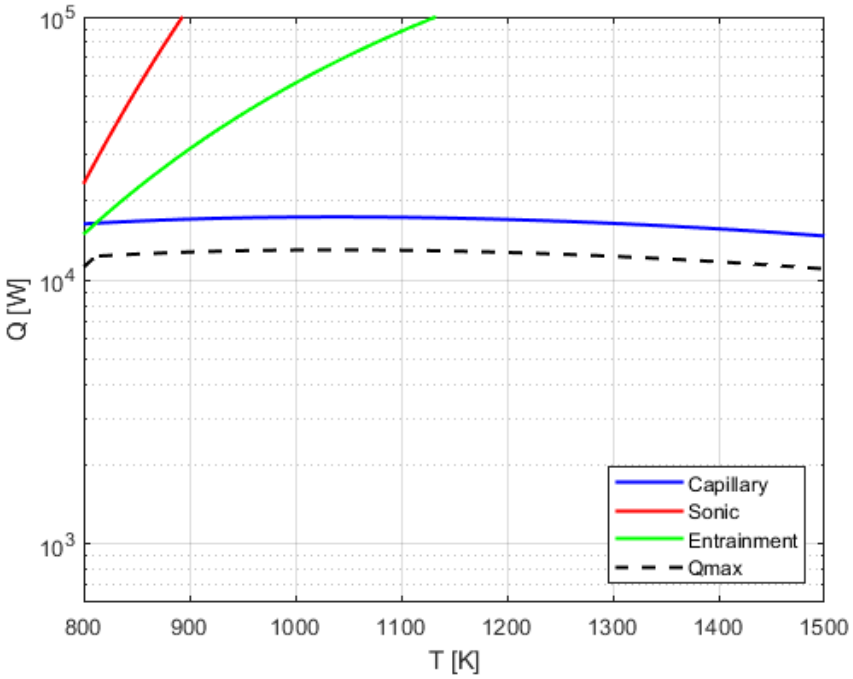

Figure 41. Optimized heat pipe operating limits.

The operating limit of heat pipe results constant above 800 K, and keeping the maximum exchangeable power equal to 75% of the capillary limit, it is obtained that the heat pipe could exchange about 12.5 kW of thermal power.

The value of thermal power obtained with the different improvements of the design is therefore lower than the operating limit with a good margin, this means that there would still room for further improvements of the design.

6. Conclusions

The ARC reactor is a promising and innovative project in the world of nuclear fusion, which has around considerable interest in the recent years. The transfer of the huge quantity of heat generated inside the reactor to a secondary fluid for electricity production through an efficient, safe and possibly economic heat exchanger still remains an open challenge. Sodium heat pipes have proved to be an excellent solution as a technology to be adopted for heat removal within ARC fusion reactor. In addition to the various advantages they offer, such as passive heat removal, the ability to avoid FLiBe freezing or tritium removal, they have demonstrated that they can exchange a significant amount of heat. A single 4 m long sodium heat pipe with an outer diameter equal to 53 cm was initially modeled with the Comsol software, and it was found that it would be able to remove 4.165 kW of thermal power from the FLiBe in the absence of fins. By applying radial fins on the external surface of the condenser, with an optimal angle of inclination of 12.3°, the thermal power has been increased up to 6.927 kW, in case air at 10 bar is used as a secondary fluid for the production of electricity inside of a Brayton cycle. The thermal power removed to the FLiBe can be increased to 8.130 kW if helium at 25 bar is used instead of air. These performances have been further improved by finding, through an exergetic analysis, the ideal thickness to use for the wick, which resulted equal to 3.1 mm, with an exchanged power equal to 8.668 kW. Further modifications can be investigated, such as carrying out a parametric analysis on the axial length to be used for the condenser and for the evaporator, or analyzing the possibility of introducing grooves on the surface of the evaporator to improve the heat exchange with the FLiBe. It was obtained that approximately 72682 heat pipes would be needed to bring the FLiBe back to the reactor inlet temperature. This number is certainly high considering the volume that the heat exchanger would occupy if it were installed, and the costs it would have.

The number of necessary heat pipes, however, can be reduced if it is considered that ARC already is designed to have a storage system which could therefore help supply the coolant at 800 K, significantly reducing the power required to be installed for the heat exchanger. The storage system could guarantee a continuous flow of the coolant at 800 K during ARC operation transients.

One possible option could be cooling the FLiBe exiting the reactor making it pass inside the heat exchanger, which would reduce its temperature to a value higher than 800 K. The FLiBe then could be stored at a temperature lower than the inlet temperature in the reactor, but reasonably higher than the melting point (e.g. 760-770 K). The temperature at the reactor inlet could be maintained equal to 800 K through a recirculation of a part of the coolant leaving the heat exchanger.

In addition, the storage could be cooled at the same time through multiple heat pipes exchanging heat by means of the natural convection with the external environment or another fluid. Heat pipes, in fact, offer the great benefit of operating passively and without any part in movement. Another great advantage arising from their use is the possibility to avoid the freezing of the molten salts through a non-condensable gas. These are some of the reasons why they have recently been studied for the passive heat removal inside molten salts reactors [19].

The success of the fusion reactors in the next years will depend, in part, on the intelligent and successfull use of process heat, and heat pipes could play a fundamental role within this context in the future.

References

[1]. https://www.iter.org/, lastseen 21/06/2021;

[2]. Kuang, A. Q., et al. "Conceptual design study for heat exhaust management in the ARC fusion pilot plant." *Fusion Engineering and Design* 137 (2018): 221-242. https://doi.org/10.1016/j.fusengdes.2018.09.007

[3]. Sorbom, B. N., et al. "ARC: A compact, high-field, fusion nuclear science facility and demonstration power plant with demountable magnets." *Fusion Engineering and Design* 100 (2015): 378-405. http://dx.doi.org/10.1016/j.fusengdes.2015.07.008

[4]. Forsberg, C., et al. "Fusion Blankets and Fluoride-Salt-Cooled High-Temperature Reactors with Flibe Salt Coolant: Common Challenges, Tritium Control, and Opportunities for Synergistic Development Strategies Between Fission, Fusion, and Solar Salt Technologies." *Nuclear Technology* 206.11 (2020): 1778-1801; https://doi.org/10.1080/00295450.2019.1691400

[5]. Segantin, S., et al. "Exploration of power conversion thermodynamic cycles for ARC fusion reactor." *Fusion Engineering and Design* 155 (2020): 111645. https://doi.org/10.1016/j.fusengdes.2020.111645.

[6]. Andreades, Charalampos, et al. "Design summary of the mark-I pebble-bed, fluoride salt–cooled, high-temperature reactor commercial power plant." *Nuclear Technology* 195.3 (2016): 223-238. https://doi.org/10.13182/NT16-2

[7]. https://inis.iaea.org/collection/NCLCollectionStore/_Public/33/011/33011260.pdf ; last access 18/05/2021.

[8]. Korn F. "Heat pipes and its applications." *Heat and Mass Transport, Project Report* (2008).

[9]. https://myheatsinks.com/heat-pipe-solutions/standard-heat-pipes/ ; last seen 18/05/2021.

[10]. Zohuri, Bahman, S. Lam, and C. Forsberg. "Heat-Pipe Heat Exchangers for Salt-Cooled Fission and Fusion Reactors to Avoid Salt Freezing and Control Tritium: A Review." *Nuclear Technology* 206.11 (2020): 1642-1658; https://doi.org/10.1080/00295450.2019.1681222

[11]. https://www.1-act.com/merit-number-and-fluid-selection/ ; last access 21/05/2021.

[12]. https://www.1-act.com/resources/heat-pipe-resources/heat-pipe-wicks/ ; last access 26/05/2021.

[13]. Panda, K. K., I. V. Dulera, and A. Basak. "Numerical simulation of high temperature sodium heat pipe for passive heat removal in nuclear reactors." *Nuclear Engineering and Design* 323 (2017): 376-385; https://doi.org/10.1016/j.nucengdes.2017.03.023

[14]. https://www.1-act.com/resources/heat-pipe-resources/heat-pipe-wicks/heat-pipe-wick-properties/ ; last seen 26/05/2021.

[15]. https://www.azom.com/article.aspx?ArticleID=7832 ; last seen 28/05/2021.

[16]. Ouyang, Fan-Yi, Chi-Hung Chang, and Ji-Jung Kai. "Long-term corrosion behaviors of Hastelloy-N and Hastelloy-B3 in moisture-containing molten FLiNaK salt environments." *Journal of nuclear materials* 446.1-3 (2014): 81-89; http://dx.doi.org/10.1016/j.jnucmat.2013.11.045

[17]. Testoni R., Segantin S., and Meschini S. "WP2: Tritium transport", Technical report in the framework of support studies for key technologies of SPARC and ARC reactors" (February 2020).

[18]. Fink, J. K., and L. Leibowitz. "*Thermodynamic and transport properties of sodium liquid and vapor*". No. ANL--RE-95/2. Argonne National Lab., 1995.

[19]. Wang, Chenglong, et al. "Transient behavior of the sodium–potassium alloy heat pipe in passive residual heat removal system of molten salt reactor." *Progress in Nuclear Energy* 68 (2013): 142-152; https://doi.org/10.1016/j.pnucene.2013.07.001